



## AN ABSTRACT OF THE THESIS OF

Emmeline Beth Altschul for the degree of Master of Science in Chemistry  
presented on July 2, 2012

Title: Transition Metal Solar Absorbers

Abstract approved:

---

Douglas A. Keszler

A new approach to the discovery of high absorbing semiconductors for solar cells was taken by working under a set of design principles and taking a systemic methodology. Three transition metal chalcogenides at varying states of development were evaluated within this framework. Iron pyrite ( $\text{FeS}_2$ ) is well known to demonstrate excellent absorption, but the coexistence with metallic iron sulfides was found to disrupt its semiconducting properties. Manganese diselenide ( $\text{MnSe}_2$ ), a material heavily researched for its magnetic properties, is proposed as a high absorbing alternative to iron pyrite that lacks destructive impurity phases. For the first time, a  $\text{MnSe}_2$  thin film was synthesized and the optical properties were characterized. Finally,  $\text{CuTaS}_3$ , a known but never characterized material, is also proposed as a high absorbing semiconductor based on the design principles and experimental results.

© Copyright by Emmeline Beth Altschul

July 2, 2012

All Rights Reserved

Transition Metal Solar Absorbers

by

Emmeline Beth Altschul

A THESIS

submitted to

Oregon State University

in partial fulfillment of  
the requirements for the  
degree of

Master of Science

Presented July 2, 2012

Commencement June 2013

Masters of Science thesis of Emmeline Beth Altschul presented on  
July 2, 2012.

APPROVED:

---

Major Professor, representing Chemistry

---

Chair of the Department of Chemistry

---

Dean of the Graduate School

I understand that my thesis will become part of the permanent collection of Oregon State University libraries. My signature below authorizes release of my thesis to any reader upon request.

---

Emmeline Beth Altschul, Author

## ACKNOWLEDGEMENTS

I would like to thank Doug Keszler for allowing me the freedom to pursue this research. I learned so much from Robert Kokenyesi and Vorra”nutch” Jieratum that this thesis is partly a tribute to their expertise. Brian Pelatt, Ram Ravichandran, and Ben Waters were wonderful team members. Of course, high quality data required the help of dozens of experts, who are too numerous for mention here. Finally, thank you to Amy Burian, Rachel Erstad, Paula and Marty Altschul and Abigail Brashler for their support and encouragement.

## CONTRIBUTION OF AUTHORS

Liping Yu and Robert Kokenyesi contributed the computational analysis and made materials suggestions. Brian Pelatt, Ram Ravichandran and Ben Waters performed the pulsed laser depositions and electron beam depositions. Brian Pelatt took the SEM images of the MnSe and MnSe<sub>2</sub> films. Ram Ravichandran measured the Seebeck coefficient of the MnSe and MnSe<sub>2</sub> films. Courtney Tanabe synthesized the phase pure marcasite powder. Synchrotron diffraction measurement was performed by Linda Lim. Andy Ritenour performed the PEC analysis of the Mn<sub>2</sub>GeSe<sub>4</sub> single crystal. Lev Zakharov solved the crystal structure of Bi<sub>1.88</sub>Mn<sub>0.88</sub>S<sub>3.75</sub>.

Experts Lev Zakharov, Josh Razink, Kurt Langworthy, Morgan Ferguson, Brady Gibbons, Sujing Xie, Jason Francis, John Donovan, Yi Liu, Shannon Boettcher and so many others helped assure that excellence in instrumentation was the standard.

## TABLE OF CONTENTS

	<u>Page</u>
Chapter 1 Introduction	1
1.1 Solar Absorbers .....	1
1.2 Absorption.....	2
1.2.1 Band Gap.....	3
1.2.2 Band Structure.....	6
1.3 Mobility and Carrier Type .....	8
1.4 Thesis.....	9
Chapter 2 Iron Pyrite	11
2.1 Introduction.....	11
2.2 Experiment .....	13
2.3 Characterization .....	14
2.3.1 Thickness, roughness and density .....	15
2.3.2 Electrical and optical properties .....	17
2.3.3 Destructive impurities in pyrite .....	20
2.4 Characterizing potential impurities in pyrite .....	28
2.5 Discussion.....	34
2.6 Conclusions.....	36
2.7 Future Work .....	36
Chapter 3 MnSe <sub>2</sub> as a solar absorber	37
3.1 Introduction.....	37
3.2 Experimental .....	40
3.3 Characterization .....	42

## TABLE OF CONTENTS (Continued)

3.4	Discussion .....	47
3.5	MnSe <sub>2</sub> as a solar absorber and future work .....	50
Chapter 4 CuTaS <sub>3</sub> Characterization and Solar Absorption Properties		53
4.1	Introduction.....	53
4.2	Calculations .....	53
4.3	Synthesis.....	56
4.4	Characterization .....	59
4.5	Results and discussion.....	62
4.5.1	Structure .....	62
4.5.2	Solar absorber candidate .....	64
4.5.3	Conclusions .....	64
4.6	Future Work .....	64
Chapter 5 Conclusions		66
Chapter 6 Appendix		72
Appendix A – Calculations.....		72
A.1	Seebeck Coefficient.....	72
A.2	Optics .....	73
Appendix B – Mn <sub>2</sub> GeSe <sub>4</sub> PEC measurements.....		75
B.1	Synthesis .....	75
B.2	PEC measurements .....	76
Appendix C – Novel Synthesis of Bi <sub>1.88</sub> Mn <sub>0.88</sub> S <sub>3.75</sub> .....		79

## TABLE OF CONTENTS (Continued)

C.1	Synthesis .....	79
C.2	Characterization.....	79

## LIST OF FIGURES

<u>Figure</u>	<u>Page</u>
Figure 1. The percent of the total solar radiation available for absorption by materials of a certain band gap as calculated using the ETR ASTM E-490 Solar spectrum[3].....	4
Figure 2. Molecular orbital diagram of a high absorbing transition metal semiconductor .....	7
Figure 3. XRD Pattern of a Solution Processed Pyrite Film, glancing incidence geometry .....	14
Figure 4. Top down SEM image of a solution processed pyrite thin film.....	15
Figure 5. SEM cross-sectional area image of a solution processed pyrite thin film .....	15
Figure 6. AFM Image of a solution processed pyrite thin film. Within the box there is a z-range of 28.4 nm and an RMS of 2.6 nm.....	16
Figure 7. XRR of solution processed iron pyrite thin film .....	17

## LIST OF FIGURES (Continued)

Figure 8. Seebeck coefficient measurement of a solution processed iron pyrite thin film. ....	18
Figure 9. The absorption coefficient of the solution processed iron pyrite films was measured by both transmission and reflection measurements that applied the Beer's Law (darker line) and ellipsometry which measures the absorption coefficient as function of the imaginary part of the index of refraction, $\kappa$ (lighter line). ....	19
Figure 10. Real and imaginary parts of the refractive index of an iron pyrite thin film.....	19
Figure 11. TEM image of a solution deposited pyrite film. Top: first platinum coating, second platinum coating (applied for TEM imaging), pyrite film, and thermal oxide .....	21
Figure 12. High resolution TEM image of a solution processed iron pyrite thin film. Two layers of platinum coat the surface. Regularly spaced, defect free, individual atoms in the pyrite lattice are visible. ....	22
Figure 13. Electron diffraction image of a small cross section of an impact fractured pyrite thin film (left) is compared to a cross section of a film processed by FIB removal (right). Even with 5 KeV energy pulses, impurity states clearly form as a result of small inputs of energy. ....	23

## LIST OF FIGURES (Continued)

Figure 14. EELS spectrum of a pyrite single crystal .....	24
Figure 15. The sulfur to iron ratio as a function of depth in a 66 nm solution processed iron pyrite thin film matches the expected to 2:1 ratio for the majority of the film. A sulfur deficiency is found in the top most 10 nm of the film.....	25
Figure 16. The calculated synchrotron radiation penetration depth through pyrite at varying incident angles. The markers are the incident angles at which the solution processed thin films were actually measured. ....	26
Figure 17. Synchrotron diffraction measurement of a pyrite thin film .....	27
Figure 18. Calculated Gibbs free energies of pyrite with respect to decomposition to $\text{FeS} + \text{S}$ or $\text{Fe}_{0.877}\text{S} + \text{S}$ as a function of temperature under a pressure of 1 atm. ....	28
Figure 19. Calculated formation energy of intermediate S-deficient phases with respect to $\text{FeS}$ and $\text{FeS}_2$ at $T = 0 \text{ K}$ .....	28
Figure 20. Pyrrhotite high crystal structure.....	29
Figure 21. Absorption coefficient of a pyrrhotite thin film .....	30

## LIST OF FIGURES (Continued)

Figure 22. Crystal structure of FeS <sub>2</sub> marcasite. The S-S bonds are shown. ....	31
Figure 23. XRD pattern of hydrothermally synthesized marcasite powder .....	33
Figure 24. Diffuse reflectance measurements of marcasite powder .....	34
Figure 25. The structure of MnSe <sub>2</sub> contains octahedrally coordinated manganese in the pyrite structure type. ....	38
Figure 26. XRD pattern of an MnSe <sub>2</sub> thin film .....	41
Figure 27. XRD pattern of an MnSe thin film on fused silica .....	42
Figure 28. SEM Image of an MnSe <sub>2</sub> film .....	43
Figure 29. SEM Image an α-MnSe film.....	43
Figure 30. Diffuse reflectance measurement of α-MnSe powder .....	44
Figure 31. Absorption coefficient of a 162 nm α-MnSe thin film on a fused silica substrate .....	45
Figure 32. Absorption coefficient measurement of a 100 nm thick MnSe <sub>2</sub> thin film on a fused silica substrate .....	46

## LIST OF FIGURES (Continued)

Figure 33. MnSe <sub>2</sub> DOS diagram.....	47
Figure 34. Band structure diagram of MnSe <sub>2</sub> .....	48
Figure 35. $\alpha$ -MnSe DOS diagram.....	49
Figure 36. Band diagram of $\alpha$ -MnSe .....	50
Figure 37. Density of states of CuTaS <sub>3</sub> as calculated using DFT theory.....	54
Figure 38. The calculated absorption coefficient of CuTaS <sub>3</sub> shows that within 0.5 eV of the band gap, greater than 10 <sup>5</sup> cm <sup>-1</sup> absorption is possible. ....	55
Figure 39. SLME calculations suggest that because of the rapid absorption turn on and >10 <sup>5</sup> cm <sup>-1</sup> absorptivity, CuTaS <sub>3</sub> has a maximum efficiency of 31%. This is close to the Shockley-Queisser[6] theoretical limit of 33% efficiency. ....	55
Figure 40. X-ray diffraction pattern of CuTaS <sub>3</sub> powder synthesized at 650°C.....	57
Figure 41. XRD pattern of a CuTaS <sub>3</sub> thin film.....	59
Figure 42. Magnetic susceptibility plot of CuTaS <sub>3</sub> . The negative susceptibility corresponds to diamagnetic behavior.....	60

## LIST OF FIGURES (Continued)

Figure 43. Diffuse reflectance measurement of $\text{CuTaS}_3$ shows a 0.9 eV band gap. This is significantly lower than the 1.37 eV band gap predicted by density functional calculations. ....	61
Figure 44. The measured absorption of a $\text{CuTaS}_3$ thin film .....	62
Figure 45. $\text{CuTaS}_3$ structure is shown with the copper sulfide tetrahedra a lighter shade than the tantalum sulfide octahedra.....	63
Figure 46. The crystal structure of $\text{Mn}_2\text{GeSe}_4$ . The manganese selenide octahedra are lightly shaded, while the germanium selenide tetrahedra are darker.....	75
Figure 47. XRD pattern of $\text{Mn}_2\text{GeSe}_4$ powder synthesized with an excess of selenium.....	76
Figure 48. Open circuit voltage PEC measurement of a $\text{Mn}_2\text{GeSe}_4$ single crystal.....	77
Figure 49. Short circuit current PEC measurement of a $\text{Mn}_2\text{GeSe}_4$ single crystal.....	78
Figure 50. SEM Image of $\text{Bi}_{1.88}\text{Mn}_{0.88}\text{S}_{3.75}$ crystals.....	80

## LIST OF FIGURES (Continued)

Figure 51. Crystal structure of  $\text{Bi}_{1.88}\text{Mn}_{0.88}\text{S}_{3.75}$ . ..... 81

## DEDICATION

To the honest pursuit of knowledge, without ego or independence

## Chapter 1 Introduction

### 1.1 Solar Absorbers

Solar cell technology has progressed significantly since Willoughby Smith reported the first photoconductor. Smith noticed inconsistent results in a test circuit for underwater cables that led to the discovery of photoconduction in selenium. About 50 years later, Albert Einstein won the Nobel Prize for explaining the photoelectric effect, but scientist's ability to predict and design photoconductors remains almost non-existent. In fact, the current solar cell technologies that incorporate Si, CdTe, and  $\text{CuIn}_{1-x}\text{Ga}_x\text{Se}_2$  (CIGS) were all discovered with only some post explanation of the underlying science.

This thesis will apply both fundamental chemistry and lessons learned through experience with known photoconductors to suggest new materials for specific use as solar absorbers in a solar cell. A systems approach to each material will be taken to best evaluate the real potential of each material. A set of design principles will be explained in the introduction and then pyrite ( $\text{FeS}_2$ ), manganese diselenide ( $\text{MnSe}_2$ ) and copper tantalum trisulfide ( $\text{CuTaS}_3$ ) will be evaluated for their potential use as a solar absorber. With the current global need for a cheaper, more efficient renewable energy supply, the conclusions of this thesis represent not only an advancement of the fundamental science of photoconductivity, but also an essential transformation to the evolution of solar technology.

## 1.2 Absorption

The primary function of a solar cell is to convert the radiation from the sun, photons with energy  $h\nu$ , into electricity. This process can be broken down into two steps. First, absorption of the light and generation of an electron-hole pair, and second, extraction of the generated carriers to produce electricity.

Absorption is really a matter of how the light interacts with a material and can be considered the difference between the total irradiation and the sum of the transmitted and reflected light through the material. In other words, when light radiation encounters a material, the energy is limited by three options: transmission, reflectance, and absorption by the material.

Transmission involves minimal interaction between the radiation and the material. The velocity and wavelength at which the light passes through the material will invariably change in accordance with the index of refraction. Phenomena such as diffraction can also occur in well-ordered material when the wavelength of the radiation is close to the size of the material [1]. In this case, the light is forced to bend in very specific ways around a material. Hence, while the radiation is affected, the material is not.

Diffuse and specular reflection, the two types of reflection, carry about the same level of interaction as transmittance, or even less so, as only the outermost layer of a material will even interact with the radiation. Specular reflectance is a predictable directional rerouting of radiation that falls on a material. Diffuse reflectance, however, is initiated by the microstructure of a material including shape, defects, and density. In fact, any surface irregularities with a depth greater than the wavelength of the incident light will cause diffuse reflectance [2].

Absorption, however, is the only interaction that fundamentally changes the radiation from one form to another. The material is similarly affected, with both kinetic and potential energies within the material changing. For example, radiative heat transfer increases the vibrational energy of atoms in a material. In this case, the overall kinetics of the system are increased. Photoconduction exists at an even more subatomic level, as the energy is absorbed by only the electrons that populate the highest energies and farthest points from the nucleus. In these valence electrons, radiation can promote an electron to a higher energy state, overcoming the attractive force of the nucleus and converting radiation into potential energy.

The initial steps of designing an absorbing material for specific use in the solar spectrum involve understanding and incorporating the structure-property relationships of band gap and transition probabilities.

### **1.2.1 Band Gap**

While about  $9.34E5 \text{ W}\cdot\mu\text{m}$  of solar radiation strikes a square meter of the earth in the wavelength range 0.310-4.429 eV [3], only the share of that radiation with a wavelength at or above the height of the band gap can be absorbed [4]. Moreover, above the band gap radiation will be extracted at the potential of the band gap, leaving the excess energy to be lost to thermal excitation[5]. Therefore, to maximize absorption within the solar spectrum, it is ideal to have a low band gap.

Figure 1 shows the percent of available solar radiation given a particular band gap. For example, a band gap of 0.9 eV is capable of capturing about 84% of the available radiation. However, available power derived from a solar absorber is a product of the current and voltage. A low band gap material will reduce the power produced by reducing the voltage of the generated current. In

a single junction solar cell, a band gap of  $\sim 1.4$  eV has been calculated to be the ideal band gap. The Shockley-Queisser theoretical maximum efficiency limit achievable with this band gap is 33% [6]. A multijunction cell, in which several semiconducting materials with a range of band gaps are stacked into a solar cell, absorbs radiation at a voltage that is more closely associated to its actual potential. This design can achieve a theoretical efficiency of 86.8% for an infinite number of layers [7], as the remaining energy is lost to unavoidable radiative recombination. New solar absorbers must be carefully designed to have a band gaps in the appropriate range for a variety of solar cell designs.

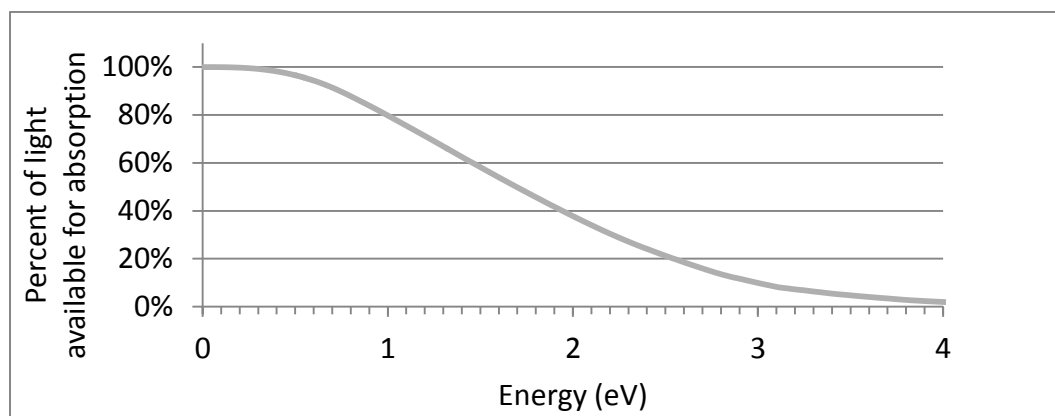


*Figure 1. The percent of the total solar radiation available for absorption by materials of a certain band gap as calculated using the ETR ASTM E-490 Solar spectrum[3]*

On a theoretical design level, predicting the band gap of a material is not straightforward. Coordination, distortion, electronegativity and bond distances within a material all play a central role in band gap determination. Qualitatively, ligand field theory can provide some guidance. For example, octahedral coordination, which leads to higher crystal field splitting, generally causes a

higher band gap than tetrahedral coordination [8]. However, this guideline assumes that the band gap is made up of the crystal field splitting within one element. In reality, band gap contributions can come from multiple elements within a binary or ternary material. Moreover, the crystal field splitting is such a product of the structure and distortions that too many exceptions exist. For example, iron pyrite, has a demonstrated band gap of 0.9 eV while pyrrhotite high, FeS, is metallic. In both materials, the iron is octahedrally coordinated with similar bond distances, but iron pyrite contains regular octahedra and FeS is characterized by distorted octahedra in a lower symmetry unit cell ( $P\bar{a}3$  versus  $Pnma$ ). A better method is to consider the interactions of polarity of the bonds and associated charge density within the unit cell. With good instincts and practice, some sense of the band gap can be developed. Complex theoretical calculations that apply density functional theory are useful methods for predicting the band gap, but even these models require correction factors and exhibit significant error [9].

Optical type is another important consideration when evaluating the absorption potential of the band gap in a semiconductor. Yu and Zunger [10] outline four band gap types by distinguishing allowed/forbidden and direct/indirect transitions from the valence band maximum to the conduction band minimum of a semiconductor. Forbidden gaps are poorly absorbing states due to parity, but still accept a certain number of promoted electrons due to orbital mixing/distortions in lattice sites. A more extended discussion of forbidden states, or forbidden transitions, is presented later in this section. Alternatively, an indirect band gap can hinder absorption by requiring a momentum change during electronic transitions. This additional momentum change, aided by lattice vibrations (phonons), decreases the likelihood of a

successful transition from the valence band to the conduction band. Hence, the best absorbers will possess a direct allowed band gap. It is important to note that indirect band gap materials, like iron pyrite, have shown excellent absorption properties. However, the energy difference between the lowest indirect and higher energy direct transitions is small.

### 1.2.2 Band Structure

Density functional theory can be used to calculate the orbitals that make up the valence and conduction band and the associated density of states (DOS), thus allowing for the determination of optical transition type near the band edge in a material and prediction of absorption (limited to direct type).

Laporte selection rules limit the probability of d-d transitions in octahedrally coordinated transition metal containing compounds because they are centrosymmetric. In this coordination, electron transitions that do not change in parity are forbidden. Only transitions of  $\pm 1$  are allowed because they involve a change in the dipole moment of the bonds. Alternatively, if the band gap is composed of tetrahedrally (non-centrosymmetric) coordinated compounds, Laporte selection rules do not limit the electronic transitions.

Spin selection rules state that transitions involving a change in the number of unpaired electron are less likely to occur. These rules apply to both octahedrally and tetrahedrally coordinated transition metals. Absorption, therefore, is also dependent on the multiplicity of the ground and excited states within the transition metal.

Finally, electrons excited in d $\rightarrow$ d or f $\rightarrow$ f energy level transitions exhibit low absorbance due to a long relaxation time of the excited electron. A long relaxation time can aid in the removal of charge in a low mobility semiconductor. s $\rightarrow$ p and p $\rightarrow$ d transitions have much shorter relaxation times, thus allowing

electrons to rapidly cycle through excitation and recombination. Therefore, the best absorbing materials involve s-p and p-d transitions which are both spin and Laporte allowed.

A calculation of the DOS of a material allows for the evaluation of the number of available states in both the valence band and the conduction band. The more states available, particularly in the conduction band, the higher the potential for absorption. Bands made up of d-orbitals tend to contain more states and have a narrower energy range than p bands, thus suggesting that the highest absorbing materials excite electrons from p orbitals to d orbitals. The trend of less states and broader energy ranges continues with decreasing quantum number.

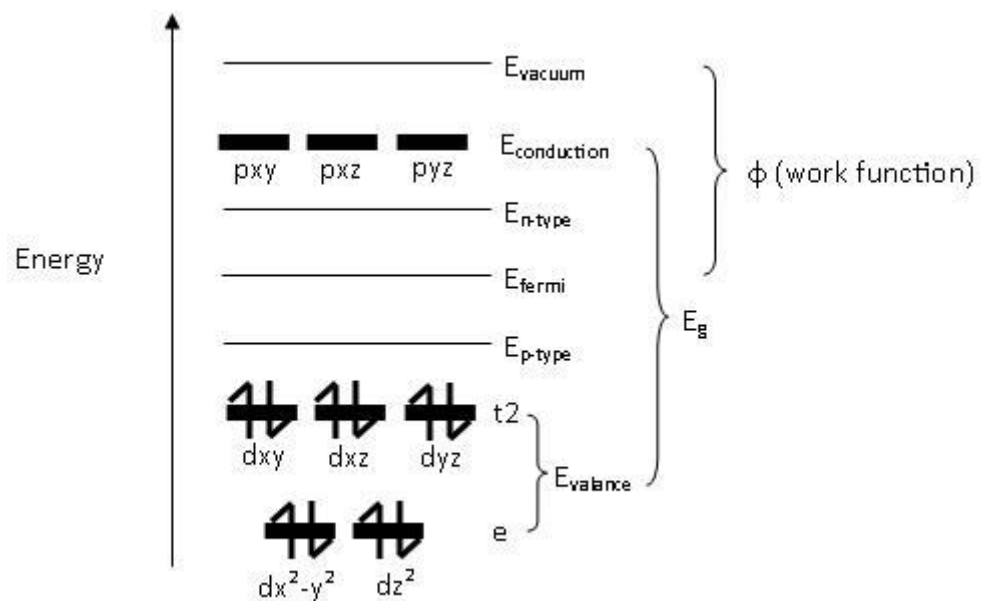


*Figure 2. Molecular orbital diagram of a high absorbing transition metal semiconductor*

The design principles discussed in this section can be summed up into the follow checklist.

- d → p transitions are spin and Laporte allowed
- high joint density of states
- $E_g = E_{\text{con}} - E_{\text{val}} \propto V_{\text{oc}}$  of the solar cell, should be in range to absorb the maximum solar radiation
- A systemic approach must be taken in the investigation of new materials. An understanding of the material as it relates to potential impurities and stability can help in understanding the real potential of a material as a solar absorber

### 1.3 Mobility and Carrier Type

While absorption is important to collecting solar energy, other factors must be considered when trying to capitalize on that absorbed energy. In designing an actual solar cell, mobility and carrier type of the solar absorber should be studied.

If the promotion of an electron generates an electron-hole pair at equal ratios, the material is known as an intrinsic semiconductor. However, solar cell architectures depend heavily on using a particular carrier type material to create diffusion or drift movement of charge out of the cell. Carrier type is the dominant method by which current is transported around a material. A carrier type can naturally form, or be doped, into a semiconductor. An excess of electrons in the conduction band is called an n-type semiconductor. In this case, the excitation of an electron generates fewer holes than in an intrinsic semiconductor. Conversely, a p-type semiconductor has an excess of holes in the valence band, the concentration of which increases with the promotion of an electron. The ratio of electrons to holes is represented mathematically by the

Fermi level energy position within the band gap, where the higher the energy, the higher the concentration of electrons in the conduction band relative to holes.

When a p-type material and n-type material are stacked, a potential is created due to electron-hole recombination at the interface. The Fermi levels “line up” as the excess electrons in the n-type material are balanced by the excess holes in the p-type material. This achieves an overall electron hole pair equilibrium within the cell while maintaining a potential energy difference between the materials. This structure is called a p-n junction. More evolved solar cell designs have been proposed, such as p-i-n, junction solar cells [12], which may improve the drift within the cell.

Mobility is the quotient of the conductivity divided by the carrier concentration within a semiconductor. The carrier concentration in a solar absorber is expected to be in the range of  $10^{14} - 10^{16} \text{ cm}^{-3}$ , while the mobility should be  $>0.5 \text{ cm}^2/\text{Vs}$ . These very general guidelines arise because too many carriers generates metallic level conduction and low mobility is connected to low carrier lifetime.

## **1.4 Thesis**

As the need for cheaper, more efficient solar technologies increases, the demand for a range of high absorbing semiconductors can be met by applying fundamental chemistry to create robust design principles for synthesizing the next generation of solar cells. To address this need, this thesis will apply the previously discussed theory to real materials in order to expand the design

principles to include practical considerations and contribute to the array of high absorbing semiconductors for solar cells.

Iron pyrite, a well-known but problematic solar absorber, along with the associated marcasite and pyrrhotite iron sulfides, have been investigated to gain a better understanding of processes that can influence the opto-electronic properties of an absorber semiconductor.  $\text{MnSe}_2$  will be suggested as an alternative to  $\text{FeS}_2$  that lacks the destructive features inherent to pyrite.  $\text{CuTaS}_3$ , a known material that has never been characterized electrically or optically, is proposed as a potential solar absorber based on predictions and experimental validation. Through this discussion, a robust set of design principles will emerge.

## Chapter 2 Iron Pyrite

### 2.1 Introduction

Iron pyrite,  $\text{FeS}_2$ , crystallizes in the  $P\bar{a}3$  structure type. Iron and sulfur have the +II and –I oxidation states, respectively, as a S-S bond creates a  $\text{S}_2^{-2}$  dimer within the structure. The octahedrally coordinated iron atoms are located at the face-centered cubic sites (fcc). Tetrahedrally coordinated sulfur atoms interpenetrate the iron lattice, suggesting a modified NaCl structure [9]. It is important to note that while all iron and sulfur bonds are of uniform length, the iron octahedra are slightly distorted, forcing the  $dx^2-y^2$  and  $dxy$  orbitals to orient off axis. The distortion lifts the degeneracies of the  $t_{2g}$  and  $e_g$  orbitals. The PBE+U DOS calculations performed by Sun et al. show the energy of the  $dx^2-y^2$  orbital is significantly lowered. Consequently, the conduction band is composed only the  $dz^2$  orbital [9].

Pyrite is a low spin structure [13] that shows n or p type conductivity [14]. Synthetic pyrite, however, is almost exclusively p-type, suggesting an iron vacancy. It has also been proposed that the p-type conductivity of synthetic pyrite has been calculated to be the result of oxygen defects that alter the charge density around the iron and potentially create a Shockley-Read-Hall recombination center [15].

In 2008, Y. Li et al. [16] published their DFT calculations on the thermodynamics of Fe-S compounds and helped explain the formation mechanisms of pyrite. Formation of pyrite via the reaction of mackinawite and gaseous  $\text{H}_2\text{S}$  is exothermic by  $-16\pm 3$  kcal/mol, while the reactions of mackinawite to hexagonal pyrrhotite are endothermic by  $13\pm 3$  kcal/mol ( $\text{Fe}_9\text{S}_{10}$ ) and  $11\pm 3$

kcal/mol ( $\text{Fe}_7\text{S}_8$ ) and exothermic to greigite by [16]. Pyrite was formed from the mackinawite at  $300^\circ\text{C}$ , but only if the mackinawite was oxidized first.

Intermediate phases of greigite and pyrrhotite were observed during the conversion. The authors point to the need for  $\text{S}^{2-}$  to be oxidized to  $\text{S}^{-1}$  in order for it to be incorporated into the pyrite structure, as the initial mackinawite contains 82% Fe(II)-S, 16% Fe(III)-S, and 2% Fe(III)-O. Since initially most of the iron is already in the +2 oxidation state, it is only available as a very weak oxidizer.

These findings point to the range of sulfur deficient binaries that are involved in the pyrite system. The solution processed pyrite is based on a reaction of FeO(OH) [17]. The iron should be a ready oxidation source. A possible mechanism for the conversion of FeO(OH) films into pyrite is the formation of sulfates followed by sulfurization of the exposed Fe(III). However, the co-formation of mackinawite, pyrrhotite, greigite, etc. are highly likely during pyrite synthesis and further support conclusions that impurities are present in pyrite thin films.

Iron pyrite has been investigated as a potential solar absorber for decades. Both experimentally and computationally, pyrite has been predicted to be a good solar absorber because of its 0.95 eV band gap and optical absorption on the order of  $10^5 \text{ cm}^{-1}$  within  $E_g+0.3 \text{ eV}$  [14]. The abundance and cost of both iron and sulfur make this compound ideal for large scale production, as iron is the fourth most abundant element in the earth's crust [18] and sulfur is a byproduct of coal mining. Additionally, the structure of pyrite has high symmetry, suggesting isotropic conduction.

Despite these properties, pyrite consistently exhibits a low open circuit voltage on the order of 150-200 meV [19]. Several theories have attempted to

explain this phenomenon. Sun et al. summarize these explanations into three categories, high concentrations of bulk and interface states that pin the Fermi level, marcasite impurities, and defects [9]. Yet theory and observation hold many discrepancies.

Therefore, in an effort to understand this system better, a comprehensive study of pyrite was undertaken in which solution processed pyrite thin films were examined by multiple overlapping techniques to best understand the cause of the low open circuit voltage. Concurrently, theorists at the National Renewable Energy Lab (NREL) calculated the energies of defects and impurity phases. Finally, characterization of marcasite and pyrrhotite were performed to better understand how these materials play into the  $\text{FeS}_2$  system.

## 2.2 Experiment

The procedure for developing solution processed iron pyrite thin films is based on methods reported by Platt [17]. Solution processed pyrite thin films were synthesized by dissolving iron nitrate and elemental iron in a 20/80 water-methanol solution over two days. The resulting solution was 0.2 M iron with a 1:2 iron to nitrate ratio. The solvent was then evaporated off under inert gas to produce an iron nitrate gel that was subsequently rehydrated and spin coated on fused silica and silicon. Multiple coats were deposited and the films were heated to 150°C for 1 minute in between each coat. Sulfurization was performed by flowing either  $\text{CS}_2$  or  $\text{H}_2\text{S}$  gas over the films at 500°C for 30 minutes to 1 hour. The resulting pyrite film is smooth and visually golden in reflection with poor substrate adhesion. XRD analysis confirmed that films are phase pure pyrite, as shown in Figure 3.

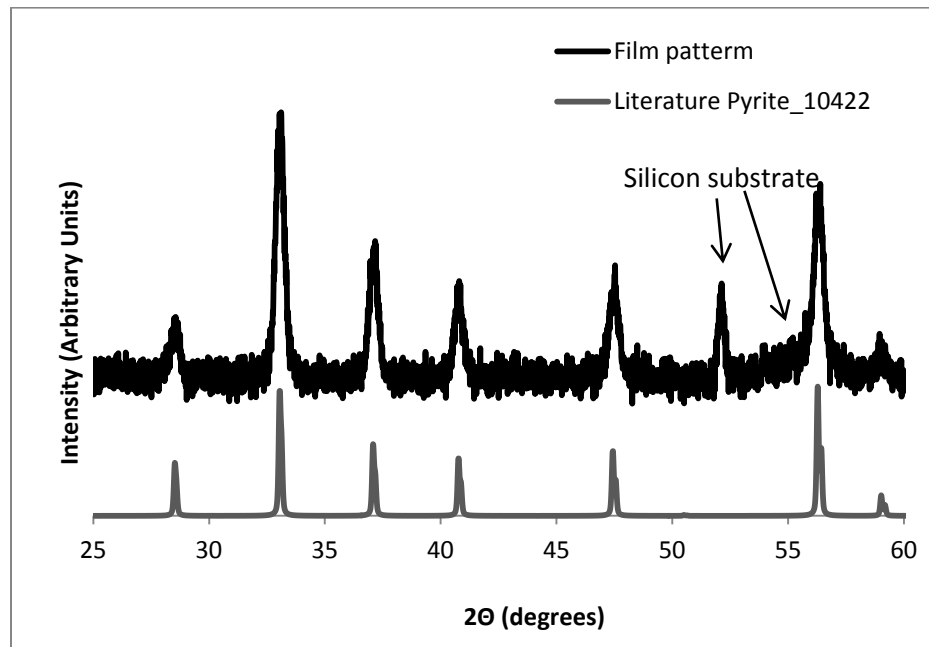


Figure 3. XRD Pattern of a Solution Processed Pyrite Film, glancing incidence geometry

### 2.3 Characterization

Scanning electron microscopy (SEM), atomic force microscopy (AFM), X-ray reflectivity (XRR), and Seebeck measurements, transmission and reflection spectroscopy and ellipsometry were all utilized to characterize the solution processed iron pyrite thin film. Each technique involved at least slightly different approaches to avoid any characteristic error that a particular method might introduce. For example, roughness was evaluated by physically dragging a silicon nitride AFM tip across the surface of a film, as well as by optical reflections in the X-ray, visible and infrared regions of the spectra.

### 2.3.1 Thickness, roughness and density

SEM images of the top down and cross-sectional areas of the solution processed pyrite thin films, Figure 4 and Figure 5, are used to measure the relationship between the number of coats and the final thickness. Each coat was found to add about 9 nm of material to the final thickness. The film density appears to be non-uniform, with areas of high and low density. The crystallinity of the films is high.

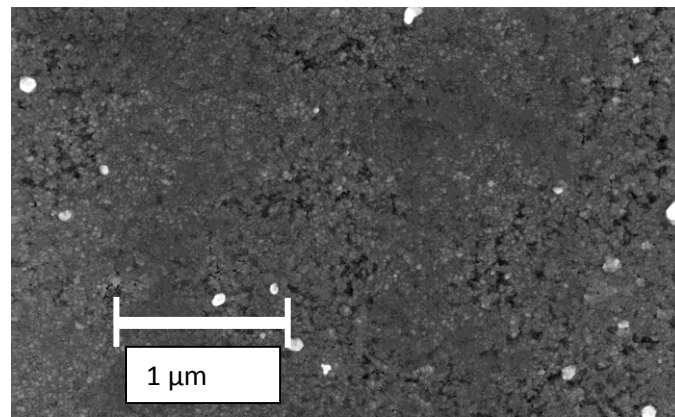


*Figure 4. Top down SEM image of a solution processed pyrite thin film.*

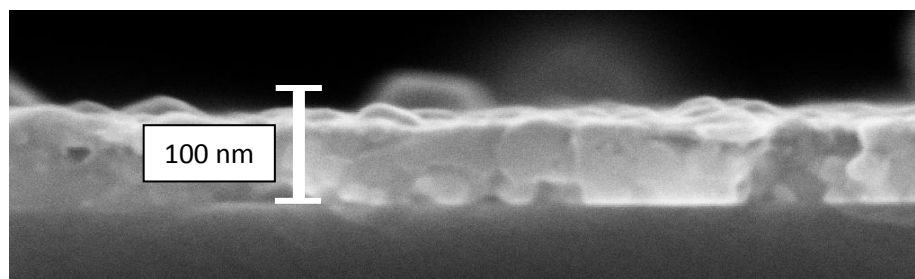


*Figure 5. SEM cross-sectional area image of a solution processed pyrite thin film*

Contact mode atomic force microscopy (AFM) images of solution processed pyrite thin films were taken to evaluate the roughness of films formed by the solution processing method. Figure 6 shows one of these films, which exhibited a z-range of 28.4 nm and RMS of 2.7 nm within the framed area. The > 1 nm roughness is characteristic of high crystallinity films. As the measured film was approximately 76 nm thick, the comparatively low z-range and continuity within the image means the voids that were visible in the top down SEM image do not extend to the substrate.

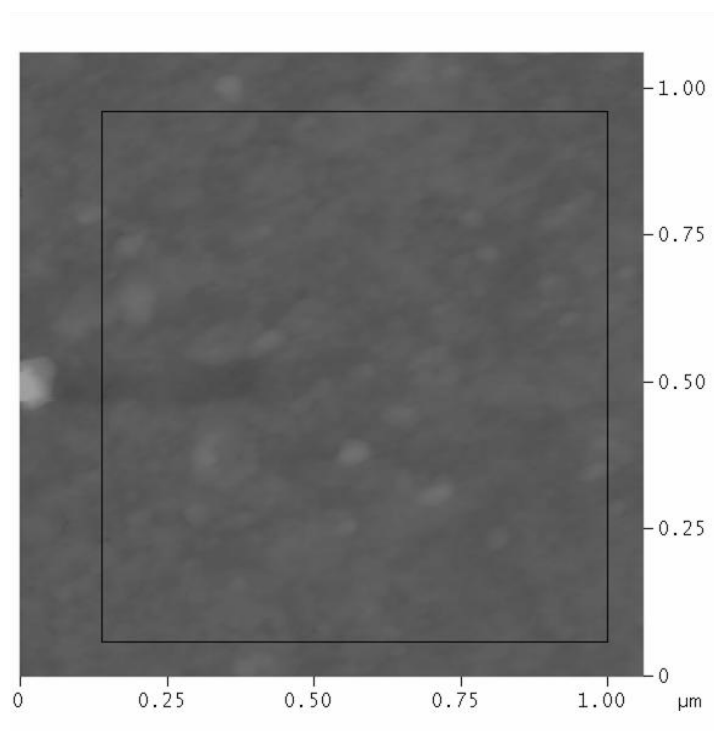


*Figure 6. AFM Image of a solution processed pyrite thin film. Within the box there is a z-range of 28.4 nm and an RMS of 2.6 nm.*

To further study thin film roughness, XRR measurements of the films are modeled yielding an estimated roughness of 2.71 nm. This roughness closely matches the RMS roughness measured by AFM, 2.66 nm. Since the thickness of the XRR model also agreed with the thickness found by SEM, the model is accepted as accurate. An XRR pattern and derived model of the solution processed pyrite film is shown in Figure 7 .

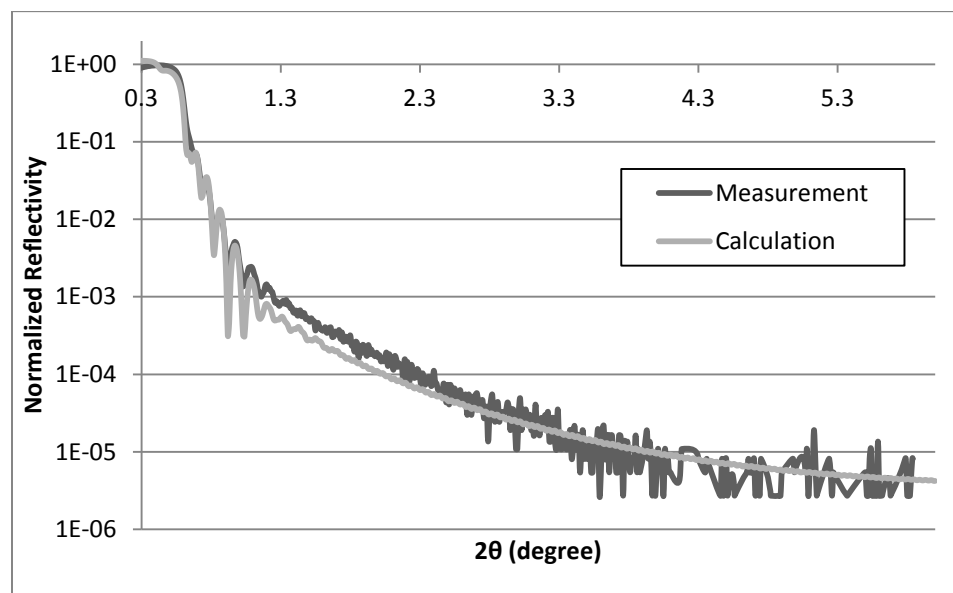


Figure 7. XRR of solution processed iron pyrite thin film

### 2.3.2 Electrical and optical properties

The measured Seebeck coefficient of solution processed iron pyrite films is +53  $\mu\text{V}/\text{K}$  which corresponds to a hole carrier concentration  $>10^{20} \text{ cm}^{-3}$ . Such degenerate carrier concentration produces metallic conductivity, suggesting that the films would not exhibit an open circuit voltage.

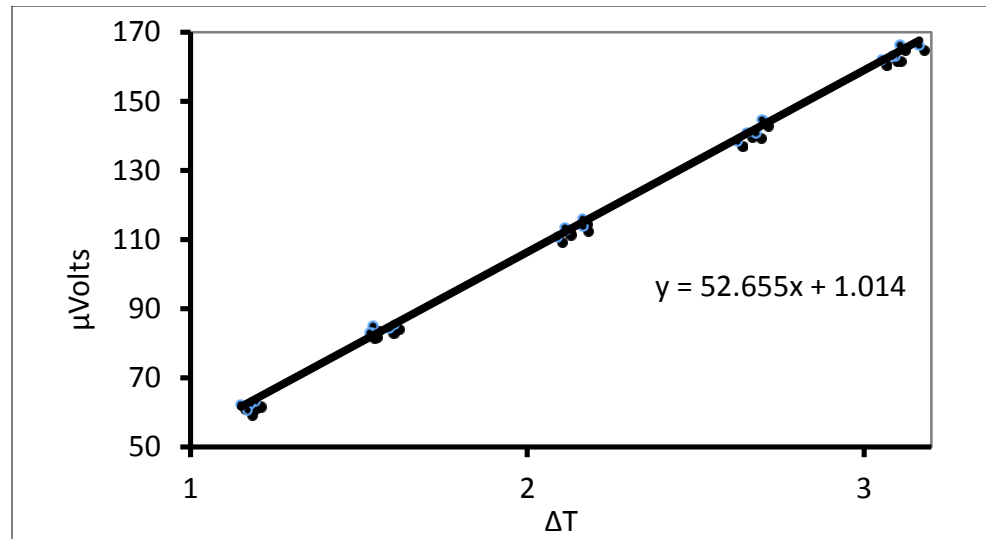


Figure 8. Seebeck coefficient measurement of a solution processed iron pyrite thin film.

Absorption by solution processed iron pyrite thin films deposited on high transmission glass substrates was evaluated by both transmission and reflection measurements and modeling of the ellipsometry spectra (Figure 9). The band gap was measured to be 1.1 eV, which closely matches the previously reported 0.95 eV band gap [14]. From the ellipsometry model, the real and imaginary parts of the index of refraction,  $n$  and  $k$  respectively, are shown in Figure 10. This ellipsometry model is supported by the thickness aspect agreement with the SEM cross-section and XRR model.

The actual maximum of absorption was found to be  $>10^5 \text{ cm}^{-1}$  within 0.6 eV of the band gap. The high sub-gap absorption suggests a large concentration of impurity states. Even the modeled absorption, which characteristically negates sub-gap absorption, shows clear absorption below the band gap.

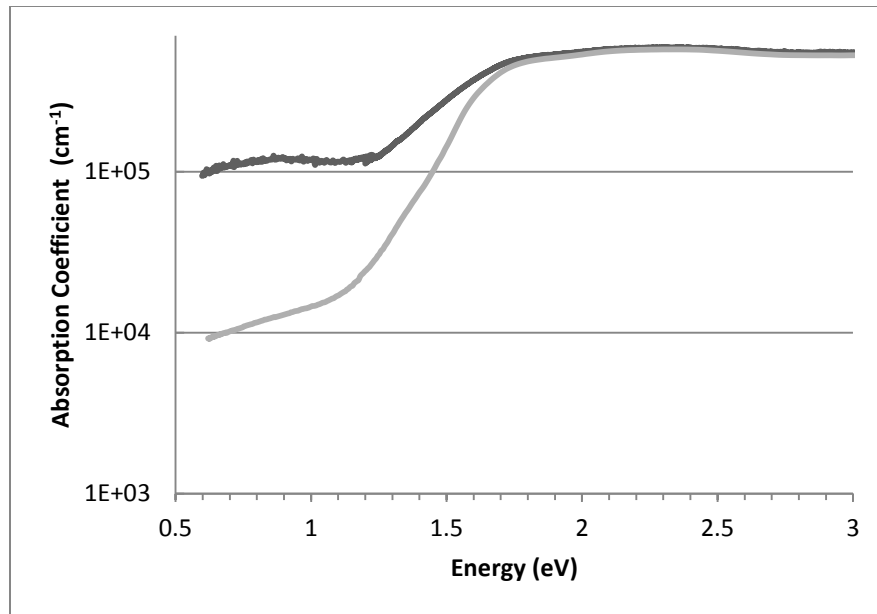


Figure 9. The absorption coefficient of the solution processed iron pyrite films was measured by both transmission and reflection measurements that applied the Beer's Law (darker line) and ellipsometry which measures the absorption coefficient as function of the imaginary part of the index of refraction,  $\kappa$  (lighter line).

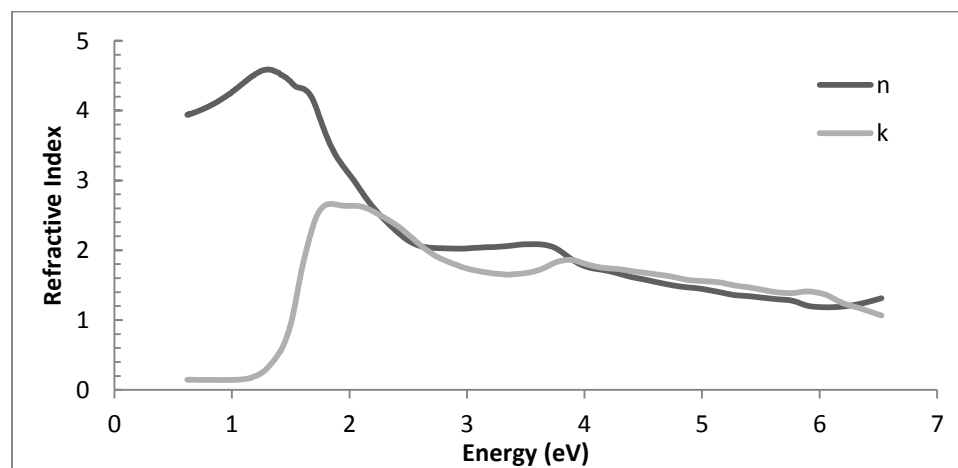


Figure 10. Real and imaginary parts of the refractive index of an iron

*pyrite thin film*

### **2.3.3 Destructive impurities in pyrite**

The unexpectedly poor electrical and optical properties were motivation for applying more sensitive and targeted structural characterization techniques to understand the nature of the films. Synchrotron diffraction, transmission electron microscopy (TEM) imaging, electron energy loss spectroscopy (EELS), electron diffraction and defect calculations are therefore used to evaluate the solution processed pyrite thin films.

Like the SEM images, TEM images of solution processed iron pyrite thin films showed a highly crystalline material. Figure 11 is one of the images taken. This sample was extracted by cutting a narrow cross-section of the film out using a focused ion beam. The narrowness of the sample allows the poor adhesion of the film on the fused silica substrate to be more clearly seen than in SEM images. This interface, combined with the aforementioned surface roughness, create a large surface area for reaction with the air. Figure 12 is a higher magnification TEM image of the solution processed pyrite thin film. At this magnification the individual atoms of the defect-free, cubic atomic structure of pyrite below the platinum coating can be seen. In fact, in the over dozen images taken of solution processed pyrite thin films that were both extracted by either a focused ion beam and by impact fracture of single crystals, only one lattice defect was found.

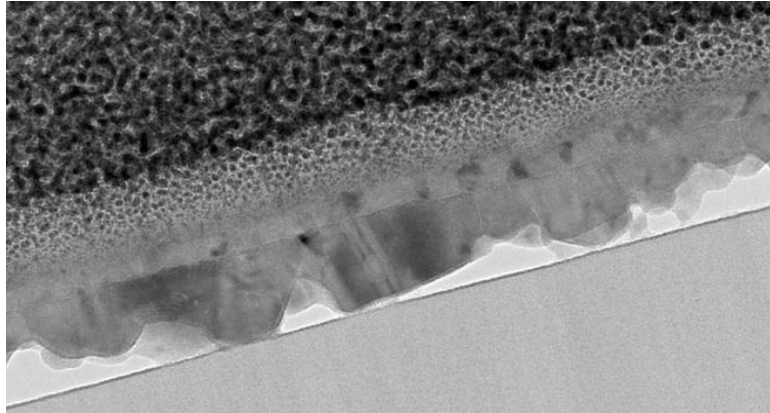


*Figure 11. TEM image of a solution deposited pyrite film. Top: first platinum coating, second platinum coating (applied for TEM imaging), pyrite film, and thermal oxide*

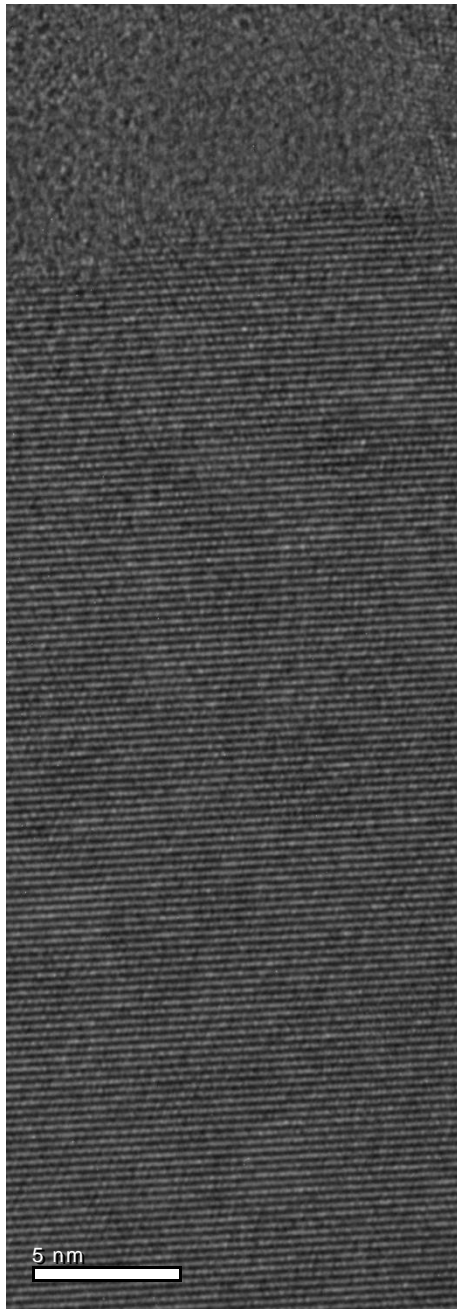


*Figure 12. High resolution TEM image of a solution processed iron pyrite thin film. Two layers of platinum coat the surface. Regularly spaced, defect free, individual atoms in the pyrite lattice are visible.*

It is important to note that careful sample preparation of iron pyrite TEM samples was imperative to attaining real data. Figure 13 shows how even small inputs of energy can destroy the phase purity of pyrite. The left electron diffraction image is of a solution processed pyrite thin film that was processed for the TEM by impact fracture. This technique involves minimal energy input into the sample. Even without spot identification, it is clear that a maximum of three species is present. The busy pattern of pyrite thin film that was FIB processed is full of impurity states, making identification impossible.

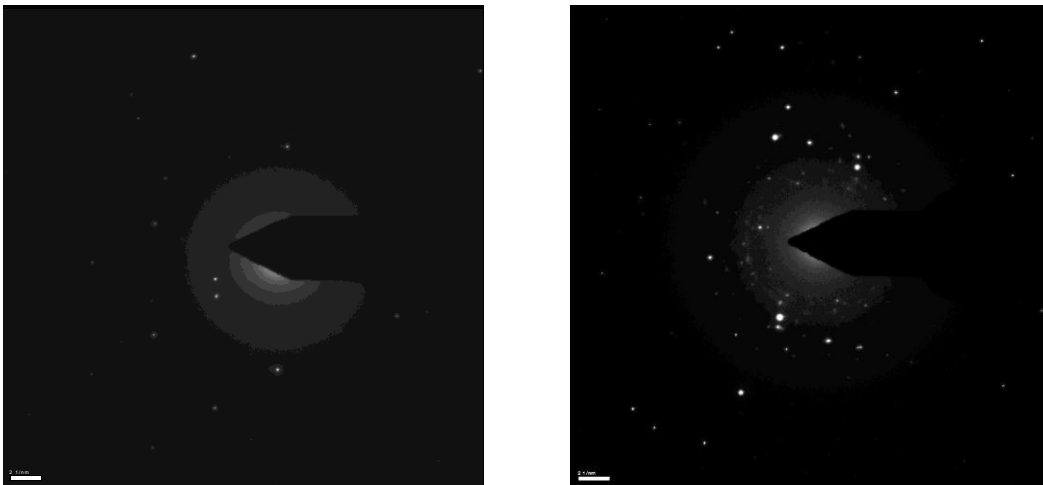


*Figure 13. Electron diffraction image of a small cross section of an impact fractured pyrite thin film (left) is compared to a cross section of a film processed by FIB removal (right). Even with 5 KeV energy pulses, impurity states clearly form as a result of small inputs of energy.*

The EELS spectrum of the same single crystal contains iron peaks at 700 eV and 717 eV at about equal proportions. These peaks are at a lower energy than traditional  $\text{Fe}_2\text{O}_3$  iron peaks [20], suggesting the presence of lower oxidation iron. This is consistent with the Fe(II) oxidation state found in pyrite.

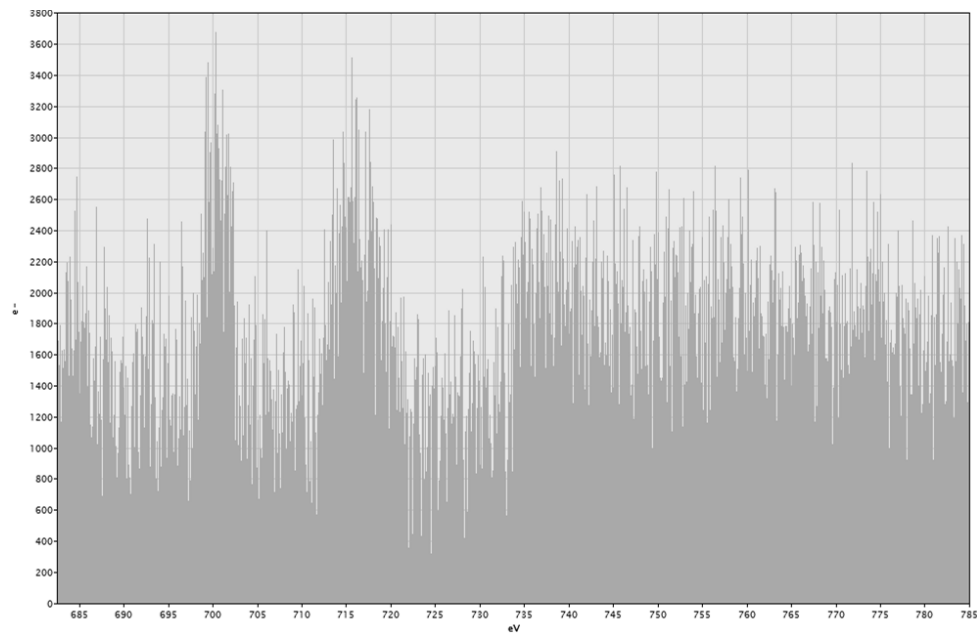


*Figure 14. EELS spectrum of a pyrite single crystal*

An electron dispersed x-ray spectroscopy measurements of the narrow film cross sections was performed and the results are shown in Figure 15. The near surface section of the film contains a sulfur deficiency, as the ratio of sulfur to iron drops to 1.4:1. The sulfur deficiency at the surface of the pyrite film could be due to iron atoms consistently being the interface atom between the platinum and the pyrite. However, with a 10 nm depth to this deficiency, it is more likely that a sulfur deficiency is present near the surface. The deeper region of the film remains at or near stoichiometry, with the deviation assumed to be within instrumental detection limits or a result of the small sample area. Therefore, the near surface region must contain amorphous sulfur deficient iron sulfides.

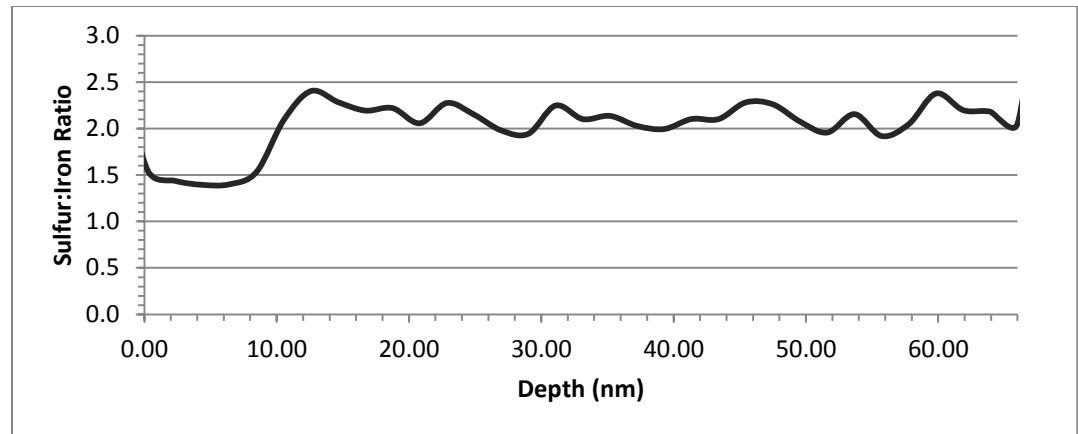


*Figure 15. The sulfur to iron ratio as a function of depth in a 66 nm solution processed iron pyrite thin film matches the expected to 2:1 ratio for the majority of the film. A sulfur deficiency is found in the top most 10 nm of the film.*

Synchrotron diffraction analysis is highly surface sensitive and depth regions as small as a few nanometers can be distinguished when near the surface [21]. This precision is lost at the critical angle, which is a function of the composition and absorption of the material being measured. The synchrotron beam used in this experiment has a wavelength of 10.2 nm (12700 eV). The absorption by pyrite at this energy was estimated to be  $100 \text{ cm}^{-1}$  and has a negligible effect on the calculated penetration depth. The density used was  $5.02 \text{ g/cm}^3$ , which is the single crystal density of pyrite. A critical angle and scattering factor were calculated and applied to find the penetration depth of the beam at various measurement points (noted by the markers) which is graphed in Figure 16.

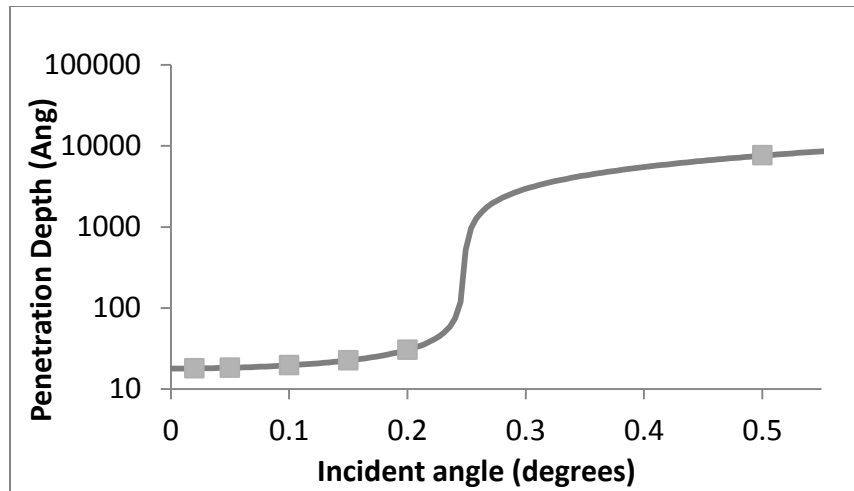


*Figure 16. The calculated synchrotron radiation penetration depth through pyrite at varying incident angles. The markers are the incident angles at which the solution processed thin films were actually measured.*

In Figure 16, the small increase in penetration depth over the incident angle range of 0 - 0.2° demonstrates the excellent surface sensitivity of this measurement. The penetration depth increases rapidly at higher incident angles, however, making it difficult to obtain an accurate profile of a pyrite thin film 3 – 300 nm from the surface. Though films ranged in thickness from 76 – 300 nm, Figure 17 only accurately reflects a profile of each film from 1.8 – 3.1 nm deep. The higher angle (0.5°) measurement shows the overall film pattern. For ease of analysis, the synchrotron radiation was converted to a typical Cu K $\alpha$  pattern using the formula  $Q = (4 \pi \cos \Theta) / \lambda$ .

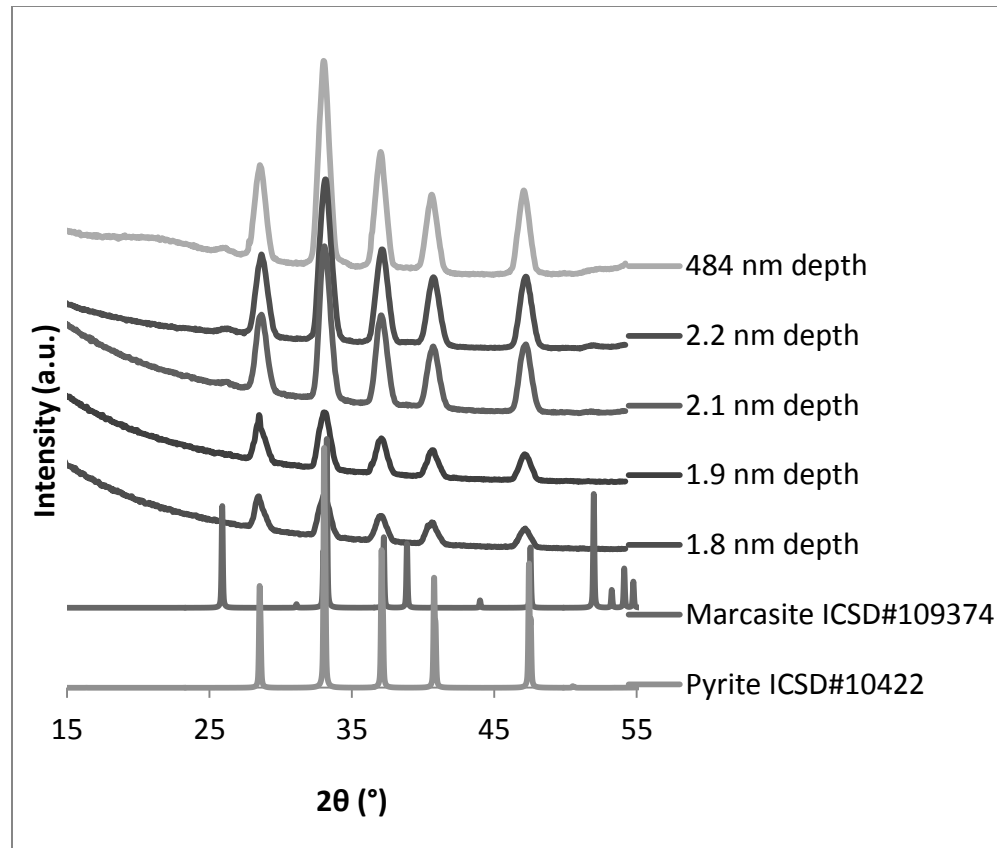


*Figure 17. Synchrotron diffraction measurement of a pyrite thin film*

Close examination the synchrotron diffraction patterns reveals minor peaks at  $25.9^\circ$  and  $52.0^\circ$   $2\theta$  angles that are characteristic of a marcasite impurity in the films. Marcasite is a lower symmetry crystal structure of  $\text{FeS}_2$  which is known to grow under the same conditions as pyrite [22].

Finally, calculations by Yu suggest that it is energetically favorable for pyrite to decompose into sulfur deficient phases [18].

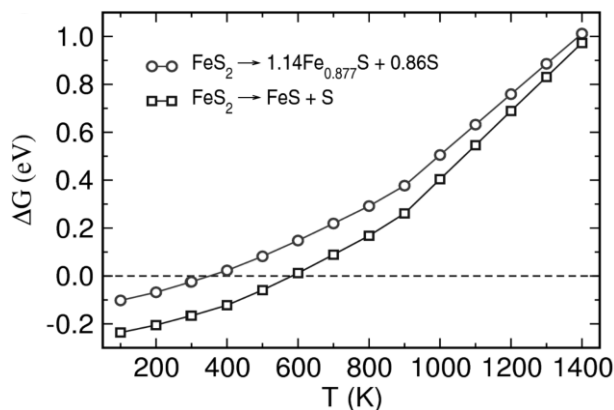


Figure 18. Calculated Gibbs free energies of pyrite with respect to decomposition to  $\text{FeS} + \text{S}$  or  $\text{Fe}_{0.877}\text{S} + \text{S}$  as a function of temperature under a pressure of 1 atm.

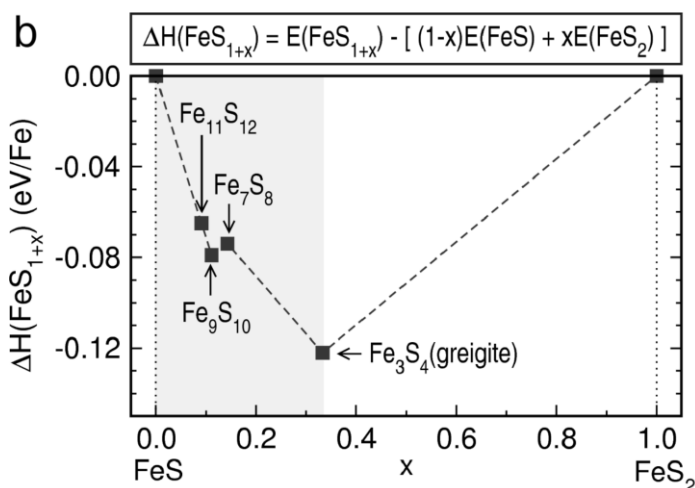


Figure 19. Calculated formation energy of intermediate S-deficient phases with respect to  $\text{FeS}$  and  $\text{FeS}_2$  at  $T = 0 \text{ K}$

## 2.4 Characterizing potential impurities in pyrite

At least 14  $\text{FeS}_x$  ( $0 < x < 2$ ) species have been reported [23] to exist in addition to many iron oxides. Unfortunately, none of the techniques applied to iron pyrite during this study were able to unilaterally identify a particular

impurity phase that disrupts the electrical properties of pyrite. That said, electron diffraction images, synchrotron diffraction, EDX, and theoretical calculations all clearly point to more species being present in pyrite thin films than are observable with a standard XRD measurement. Investigation of every potential impurity is beyond the scope of this thesis so the most likely impurities, pyrrhotite and marcasite are briefly investigated to understand how their presence would influence a pyrite thin film.

Pyrrhotite, FeS, is a frequently observed impurity in the development of a synthetic procedure for FeS<sub>2</sub> thin films. The particular pyrrhotite, pyrrhotite high, that was frequently found crystallizes in the Pnma space group. While not the only potential impurity in pyrite, this species forms prominently in growth conditions similar to pyrite. Thus, it is considered a likely cause of the sulfur deficiency in the EDX results and the impurities shown in the electron diffraction image.

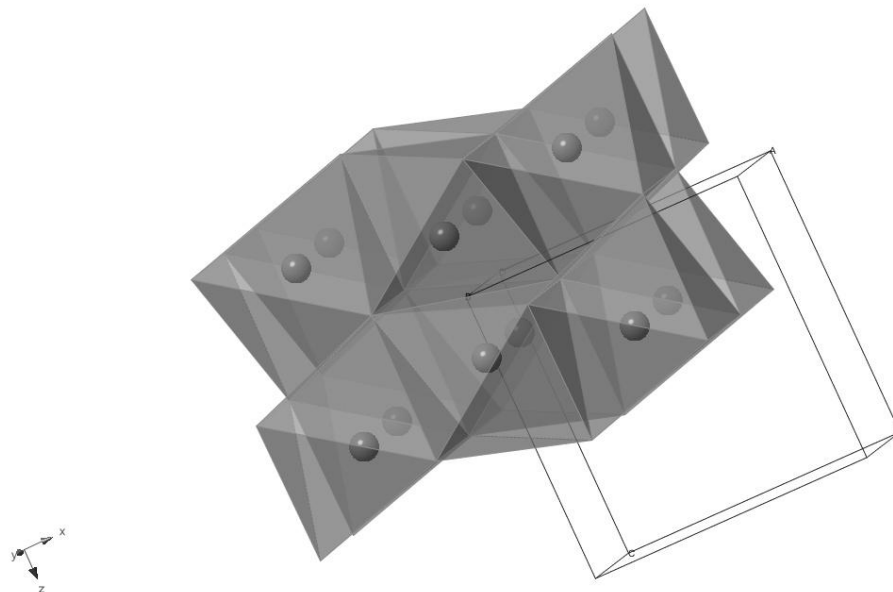


*Figure 20. Pyrrhotite high crystal structure*

Pyrrhotite high consists of face sharing octahedra in a continuous lattice. The high degree of interaction among the octahedra could be the cause of its reportedly high conductivity [24]. A thin film of pyrrhotite was synthesized by the same method as the solution processed pyrite thin films except with a process temperature of 300°C. Figure 21 shows the estimated absorption coefficient of an approximately 50 nm thin film. Given the high absorption coefficient, the amount of pyrrhotite needed to achieve significant absorption below the pyrite band gap is quite small. XRD analysis cannot detect low level and/or amorphous impurities, making this a reasonable, but hard to detect, impurity.

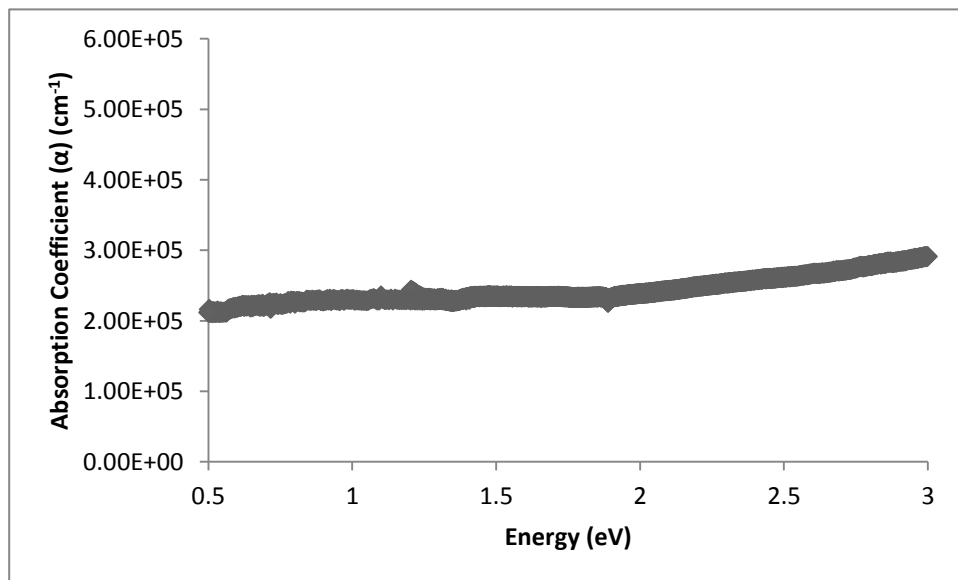
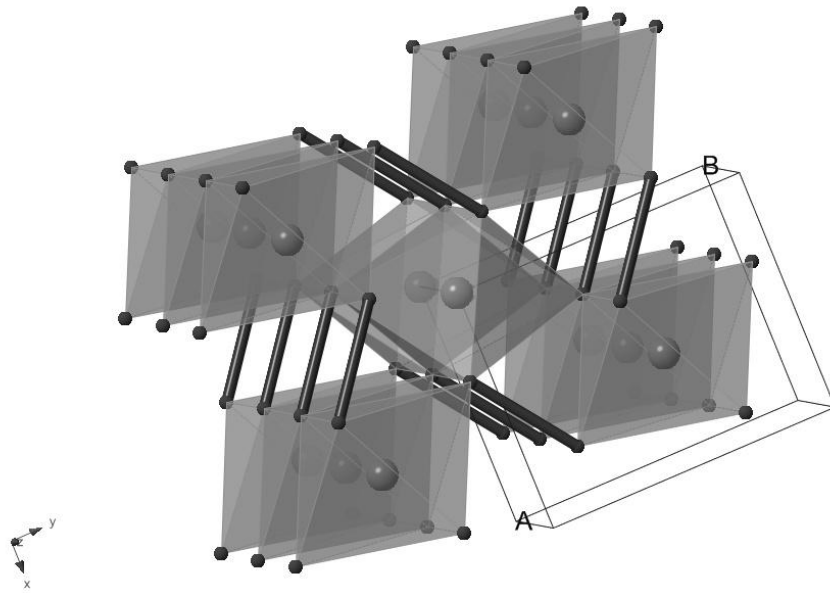


Figure 21. Absorption coefficient of a pyrrhotite thin film

Marcasite is another common impurity in synthetic pyrite, and is readily synthesized in a manner similar to pyrite but with only slight variations to the reactants [22]. In fact, marcasite contains similarly distorted iron octahedra and

sulfur tetrahedra with a  $S_2^{-2}$  dimer. The material, however, crystallizes in the space group Pnmm. The structure is most closely related to a  $CaCl_2$ , as it is composed of rectilinear columns of edge-shared octahedra that are joined in the a-b plane by corner sharing [25]. The bond distances of the Fe-S bonds in marcasite range from  $2.2305 \pm 0.0158$  to  $2.2506 \pm 0.0092$  Å [26] while pyrite has Fe-S bonds of a uniform  $2.2687 \pm 0.0003$  Å [27]. The most obvious distinction between the properties of marcasite and pyrite are that conduction is expected to be primarily along only the c axis and a much higher degree of isolation is experienced between columns.



*Figure 22. Crystal structure of  $FeS_2$  marcasite. The S-S bonds are shown.*

The similarities between pyrite and marcasite led Sun et al. to calculate the electronic structure and band gap of marcasite from first principles theory [9]. They concluded that marcasite should exhibit a band gap around 1.2 eV and lack any gap states that would be destructive to pyrite photovoltaic performance.

These calculations contrast sharply with the experimental findings of Jagadeesh and Seehra. They used a temperature dependent electrical resistivity measurement to determine that the band gap of marcasite is 0.34 eV [28]. This energy is low enough to activate carriers, but not high enough to exhibit traditional semiconducting properties.

In an effort to settle this discrepancy, phase pure marcasite powder was synthesized and the diffuse reflectance was measured. The synthesis of phase pure marcasite is non-trivial despite marcasite being readily found in nature. Hydrothermal growth mechanisms were found to be the most successful synthesis method. Phase pure marcasite was attained by creating a solution of 0.01 M  $\text{H}_2\text{SO}_4$ , 0.18 M  $\text{FeSO}_4$  and 0.16 M of elemental sulfur in a 23 mL Teflon vessel. The vessel was filled to about two-thirds capacity, as per the manufacturers' instructions, and sealed in the appropriately sized bomb shell casing. The entire apparatus was heated at a rate of  $1^\circ\text{C}/\text{min}$  to  $200^\circ\text{C}$ . After 1440 minutes, the vessel was allowed to cool at  $1^\circ\text{C}/\text{min}$ . A Buchner funnel was used to filter the resulting powder and flakes. After grinding, the material was found to be phase pure marcasite by XRD analysis (Figure 23).

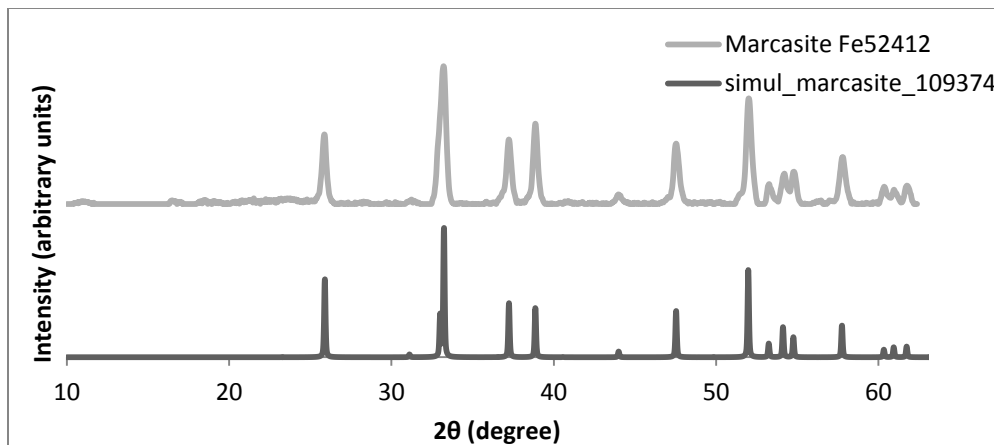


Figure 23. XRD pattern of hydrothermally synthesized marcasite powder

Diffuse reflectance measurements of the marcasite powder, shown in Figure 24, do not show a band gap in the range of 0.5 eV to 5.0 eV. Instrumentation limitations do not allow for measurement of the spectra around 0.34 eV, so this measurement was unable to confirm the previously reported band gap. Ellipsometry or transmission/reflection spectroscopy measurements would provide more conclusive evidence of the band gap, and these experiments are underway.

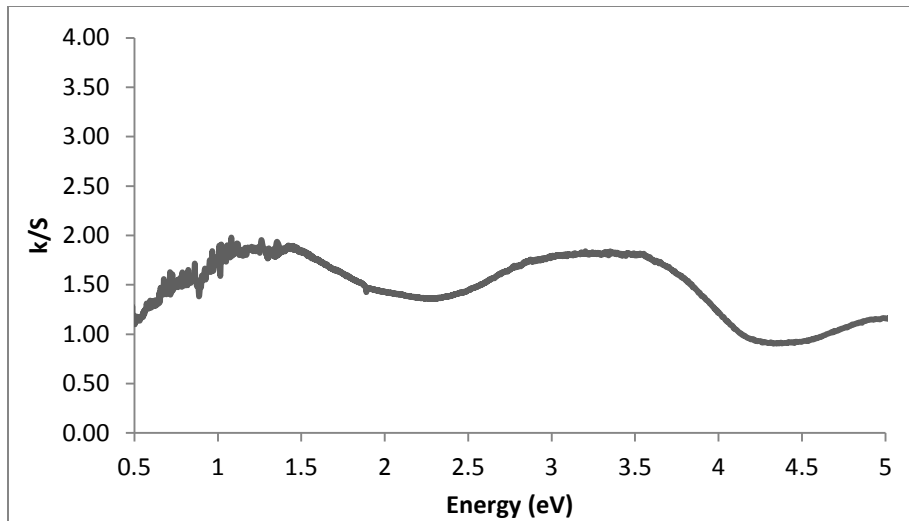


Figure 24. Diffuse reflectance measurements of marcasite powder

## 2.5 Discussion

Based on the characterization of solution processed pyrite thin films, strong evidence exists for sulfur deficient impurities readily forming on iron pyrite. These impurity materials could cause of the sub-gap absorption in pyrite.

The clearest evidence of sulfur loss at the surface is shown in the EDX cross section of a solution processed pyrite thin film. The first 10 nm have significantly lower sulfur to iron ratios than the remainder of the film. Any sulfur loss results in either amorphous or crystalline  $\text{FeS}_x$  and/or oxides species on the surface, typically not observable by XRD. The free energy of formation and heat of formation calculations show that sulfur deficient species are energetically favorable with only a small input of energy. During FIB, an excellent example of a small input of energy in a vacuum environment, at least one new material was observable by electron diffraction as pyrite lacks that many reflection peaks.

While identification of this species could not be made, this qualitative data still suggests significant reactivity of pyrite in an oxygen free environment.

Alternatively, surface sensitive synchrotron diffraction analysis suggests marcasite impurities in films that have only been exposed to ambient conditions. Since marcasite readily intergrows with pyrite, this impurity is likely to have formed during synthesis, but been undetectable by laboratory scale XRD analysis. The exact semiconducting properties of marcasite are debated so the effect of this impurity on the optical and electrical properties of pyrite is unknown.

Sulfur loss and surface oxidation in pyrite have been reported in multiple other studies. X-ray photoelectron spectroscopy (XPS) studies show a loss of sulfur upon exposure of cleaved surfaces to air [29]. Nesbitt et al.[30] reviewed several XPS studies of pyrite surfaces, including their own and added synchrotron XPS evidence of surface decomposition. Experiments were performed on freshly fractured pyrite surfaces under vacuum. Detailed SXPS analysis indicated that the surface consisted mainly of  $\text{Fe}^{2+}$  and  $\text{Fe}^{3+}$  sites. These ions are difficult to detect without rapid sampling times on the order of  $10^{-15}$  s because of the electron hopping between iron species. These ions are created independently of  $\text{S}^{2-}$  and under vacuum these highly reactive species remain stable.

Previous XPS studies performed in air demonstrate that fractured surfaces will contain  $\text{Fe}^{3+}$  moieties within 24 hours of exposure [30]. However, sulfur exposed by fracturing pyrite will rapidly oxidize. Schaufuß et al.[29] applied SXPS techniques to the surface of pyrite and found that within one minute of exposure to air, 80% of the  $\text{S}^{2-}$  on the surface oxidized into a sulfate. Buckley and Woods reported similar findings [31].

## 2.6 Conclusions

Pyrite makes a very poor solar absorber because even if it can be synthesized into a phase pure thin film, it readily breaks down when exposed to ambient. The work presented in this thesis is mostly a qualitative exploration of the potential decomposition of pyrite, but when combined with years of previous research, makes a strong case for a highly reactive, but defect free, material. Thus, the range of reported chemistries and impurity states that occur within pyrite make it a rich material to research, but an ultimately impractical material for solar cells.

## 2.7 Future Work

In performing this research several questions arose about the nature of materials related to iron pyrite. Significant literature exists about marcasite in geological formations, but still very little is known about its optical and electrical properties. Synthesis and characterization of a marcasite thin film and/or single crystal could answer some interesting theoretical questions about the structure-property relationships of iron sulfides.

The difficulty in obtaining a single phase material may also be considered an impetus for further work on related structures. The olivine structure of  $\text{Fe}_2\text{-X-}\text{Ch}_4$  ( $\text{X} = \text{Si, Ge}$ ;  $\text{Ch} = \text{S, Se}$ ) compounds has been suggested as a stable material with similar absorption properties [18]. However other alternatives exist, such as  $\text{MnSe}_2$  that is described in the next section.

## Chapter 3 MnSe<sub>2</sub> as a solar absorber

### 3.1 Introduction

The previously discussed impurity phases that disrupt the semiconducting properties of iron pyrite make this material a poor candidate for use as a solar absorber. However, using this system as a model to learn about the structure property relationships that give rise to high absorption and as a warning about potential electrical killers, MnSe<sub>2</sub> is proposed as a suitable alternative material. While the magnetic properties of MnSe<sub>2</sub> have been studied [32], no report has been found that characterizes the optical or electrical properties of this material.

MnSe<sub>2</sub> crystallizes into the same NaCl-like structure and  $P\bar{a}3$ - space group as iron pyrite, but lacks the chalcogenide deficient phases of iron pyrite.

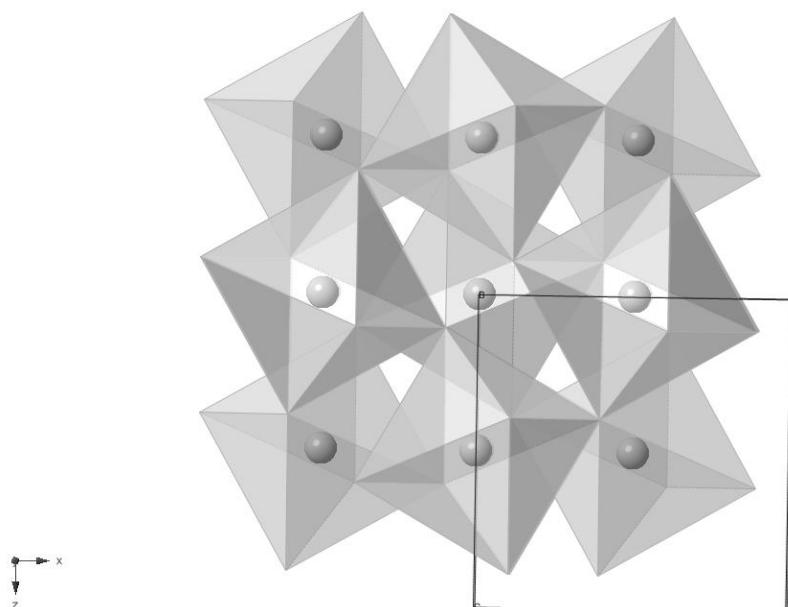


*Figure 25. The structure of  $MnSe_2$  contains octahedrally coordinated manganese in the pyrite structure type.*

The lack of non-integer stoichiometries in the Mn-Se system can be explained by the lower energy of formation of the Mn(II) oxidation state,  $-2.36 \text{ NE}^\ominus$ , compared to Mn(III),  $-0.86 \text{ NE}^\ominus$ . For iron, the formation energy of Fe(II) is  $-0.88 \text{ NE}^\ominus$  while Fe(III) has a formation energy of  $-0.4 \text{ NE}^\ominus$  under acidic conditions [8]. Thus, Mn(II) is a more energetically stable oxidation state than Fe(II). While these energies of formation were measured for acidic solutions, they no less apply to the acidic solid solutions of inorganic chemistry.

In fact, only three other binary Mn-Se systems have been reported (vs. the 14 of  $FeS_x$ ) [23].  $\alpha$ -MnSe is a cubic NaCl structure with regular octahedrally coordinated manganese and selenium. The Mn-Se bond distance in this Fm3-m structure is  $2.73 \text{ \AA}$  [33]. It is closely related to the  $MnSe_2$  structure. By interchanging the  $Se_2^{-2}$  dimers with a single selenium in the middle of the edges,

the  $\alpha$ -MnSe structure can be obtained [32].  $\beta$ -MnSe is a sphalerite structure with regular tetrahedrally coordinated manganese. The Mn-Se bond distance is 2.52 Å [33].  $\beta$ -MnSe has a band gap of 3.3 eV [34] but given that it only forms above 500°C, this is an unlikely impurity in an MnSe<sub>2</sub> film. One other MnSe phase has been reported, the  $\gamma$  hexagonal structure, but it only forms at high pressure and high temperature [35].

The low temperature MnSe phase,  $\alpha$ -MnSe, is the most likely impurity phase in MnSe<sub>2</sub> so gaining an understanding of its optical and electrical properties can help in understanding the real promise of MnSe<sub>2</sub>.  $\alpha$ -MnSe is a semiconductor, though the actual band gap is controversial in the literature. Early reports describe  $\alpha$ -MnSe as an insulator [36], but they lack supporting evidence for this conclusion and had admittedly poor agreement between samples when measuring the optical properties. Thanigaimani and Angadi reported an absorption edge ranging from 0.16 -1.124 eV, but also gave strong evidence that their films contained significant phase impurity [37]. Heimbrodt et al. described the optical properties of a mix of  $\alpha$ -MnSe and  $\beta$ -MnSe at a layer thickness of only 4 nm. They characterized the Tanabe-Sugano transitions at low temperatures, but noticed changes in transitions with increasing temperature [34].

Since no report has been found that characterizes the optical or electrical properties of MnSe<sub>2</sub> and controversy still exists about the optical properties of  $\alpha$ -MnSe, characterization of these materials is needed in order to understand the hypothesized value of MnSe<sub>2</sub> as a solar absorber.

### 3.2 Experimental

$\alpha$ -MnSe powder was synthesized by combining stoichiometric amounts of manganese and selenium in an air evacuated ( $10^{-3}$  torr) sealed fused silica tube. The tube was heated at  $2^{\circ}\text{C}/\text{min}$  to  $650^{\circ}\text{C}$ . Two to four days later, the tube was allowed to cool uncontrolled or at about  $3^{\circ}\text{C}/\text{min}$ . The resulting powder was confirmed to be phase pure  $\alpha$ -MnSe by XRD analysis.

An 81% dense  $\alpha$ -MnSe target was made by first cold pressing  $\alpha$ -MnSe powder into a pellet. The pellet was placed into a hot isostatic press and cycled through vacuum and argon cycles to remove oxygen from the chamber. Then 15,000 psi of argon was applied to the target which was then heated to  $1000^{\circ}\text{C}$  over the course of 4 hours with a final pressure of 25,000 psi. After 3 hours, the target was allowed to cool over the course of 3 hours to  $150^{\circ}\text{C}$ , at which point the pressure was released to atmospheric. The final  $125^{\circ}\text{C}$  of cooling occurred because of the pressure release.

A  $\text{MnSe}_2$  film was synthesized by electron beam deposition from an  $\alpha$ -MnSe target at room temperature onto a fused silica substrate. This film was then annealed in a selenium atmosphere in an air evacuated ( $10^{-3}$  torr) sealed fused silica tube at  $400^{\circ}\text{C}$  for one hour. A ramp rate of  $2^{\circ}\text{C}/\text{min}$  and cooling rate of  $3^{\circ}\text{C}/\text{min}$  were found to be ideal for generating excellent film crystallinity and selenium condensation. The XRD pattern of the resulting film, shown in Figure 26, matches previously reported  $\text{MnSe}_2$  XRD patterns and lacks extraneous peaks.

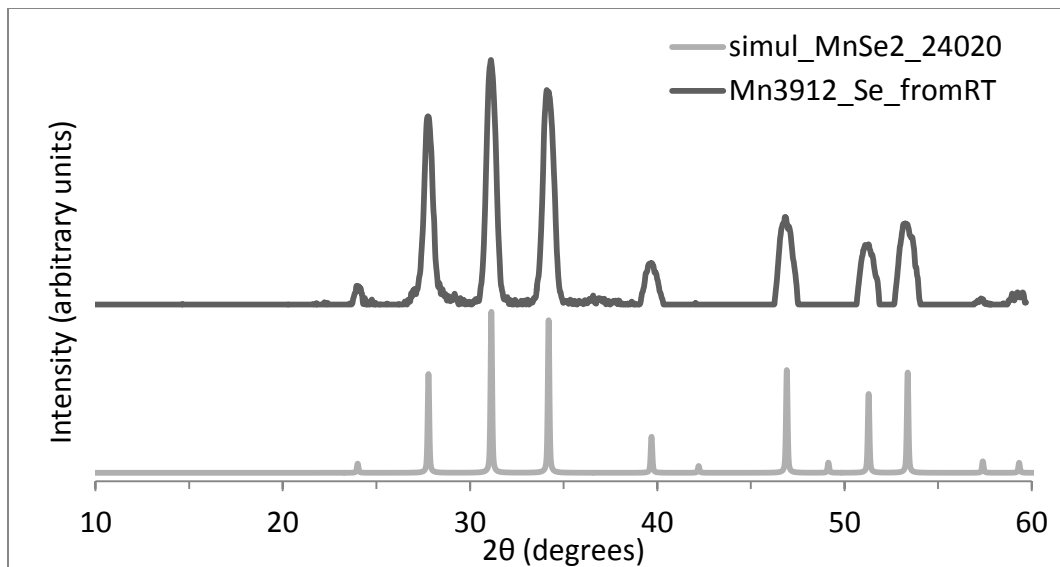


Figure 26. XRD pattern of an MnSe<sub>2</sub> thin film

An  $\alpha$ -MnSe film was synthesized similarly, but at an electron beam deposition temperature of 300°C. The heated substrate better crystallizes the  $\alpha$ -MnSe film, resulting in the maintenance of a phase pure  $\alpha$ -MnSe film even after a subsequent 400°C anneal in selenium. The XRD pattern of the resulting film, shown in Figure 27, is identical to previously reported patterns and lacks extraneous peaks.

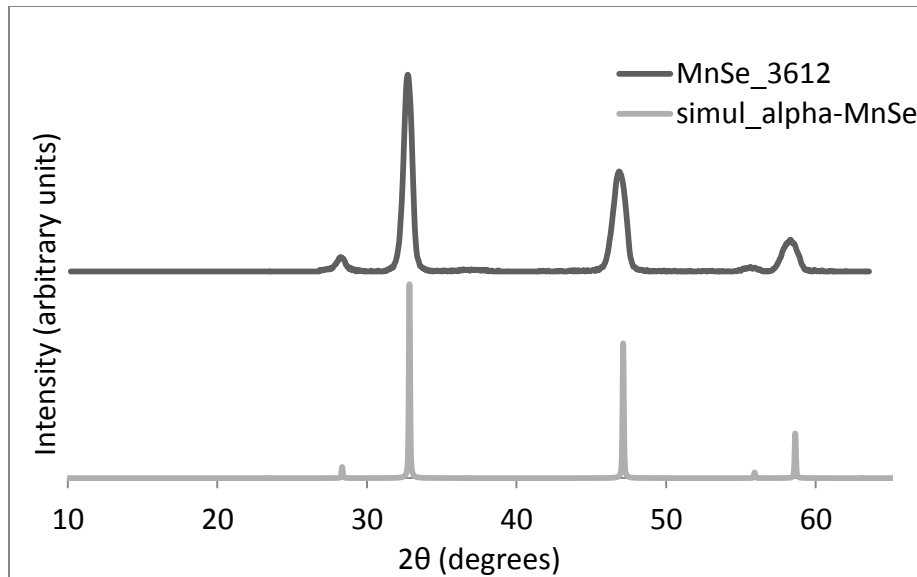
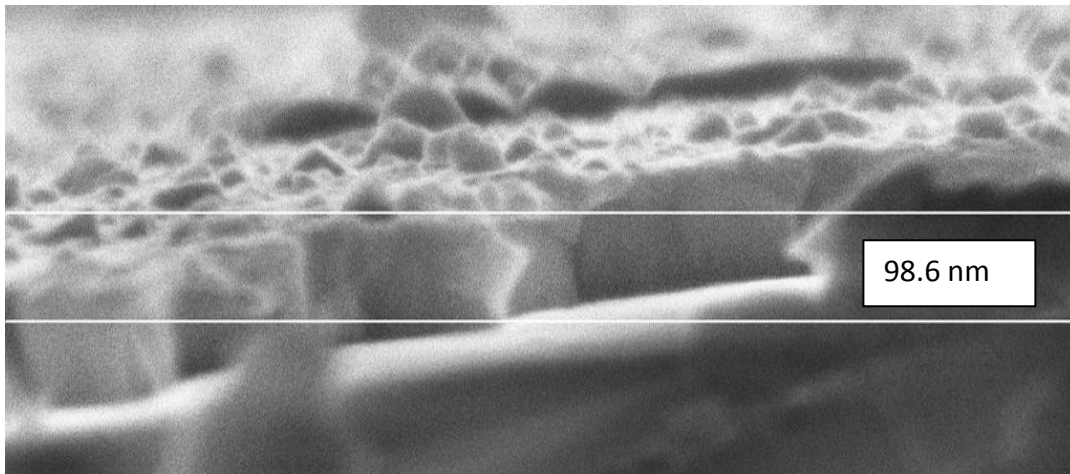


Figure 27. XRD pattern of an MnSe thin film on fused silica

### 3.3 Characterization

SEM images of cleaved cross sections of both the MnSe<sub>2</sub> and α-MnSe films were taken to evaluate their density, thickness, roughness, crystallinity and conductivity. Figure 28. SEM Image of an MnSe<sub>2</sub> film is a cross section a MnSe<sub>2</sub> film that clearly demonstrates high crystallinity and density in a ~100 nm film. No charging occurred during the imaging, suggesting that there is at least some conductivity in the film. Roughness, as can be expected in a highly crystalline film, is on the order of several nanometers. Significant roughness can disrupt optical measurements by scattering the reflected light, thus artificially increasing the absorption coefficient.



*Figure 28. SEM Image of an MnSe<sub>2</sub> film*

The SEM image of the  $\alpha$ -MnSe film shows a smoother, more uniform film, while maintaining the high degree of crystallinity, density and charge-free imaging of the MnSe<sub>2</sub> film image. The gap between the substrate and the film could be a result of the strain caused by the cleaving.

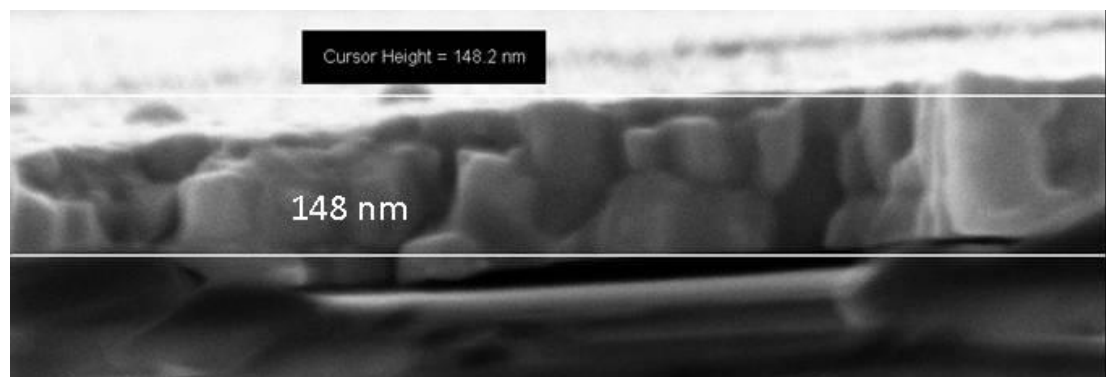


*Figure 29. SEM Image an  $\alpha$ -MnSe film*

Diffuse reflectance measurements of  $\alpha$ -MnSe powder, shown in Figure 30, establish a rapid turn on of absorption at 1.77 eV. Correspondingly, a 162 nm

thin film of  $\alpha$ -MnSe on fused silica has a rise in absorption around 1.8 eV that can be seen in Figure 31. However, the real takeoff of the absorption coefficient is around 2.3 eV. The grey coloration of the powder supports a lower band gap, as all of the high energy light should be absorbed. Therefore, the discrepancy in band gap between the diffuse reflectance and the film highlights the slow turn of absorption in  $\alpha$ -MnSe resulting from the indirect gap.

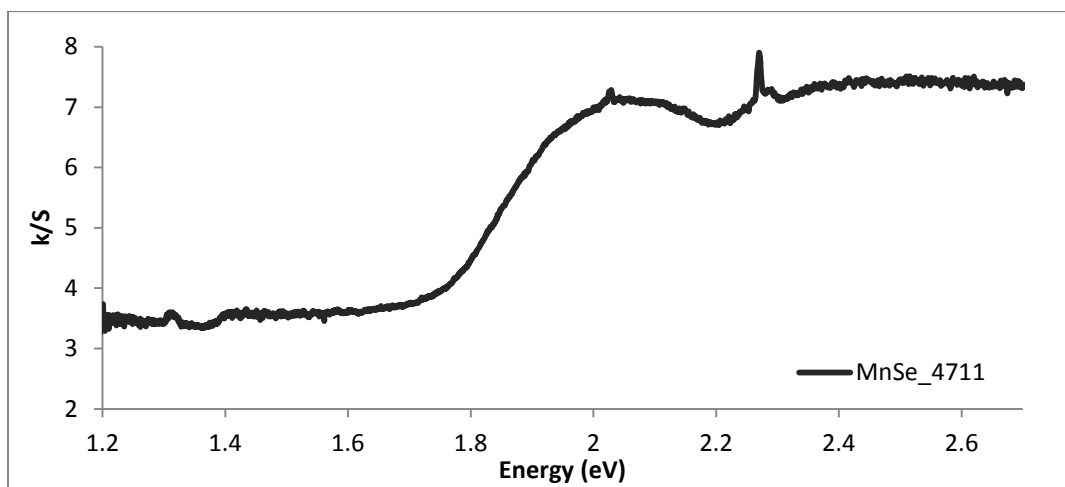
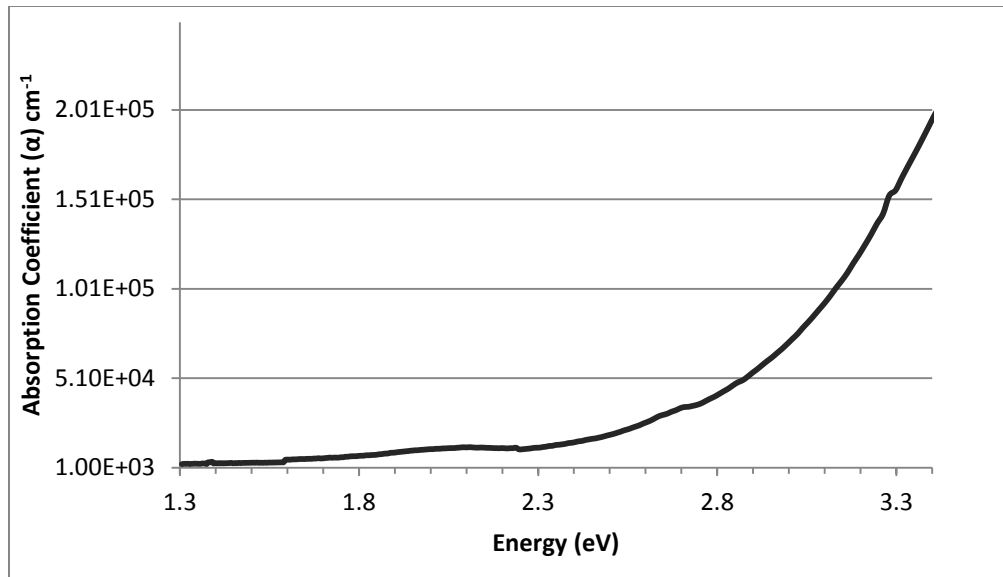


Figure 30. Diffuse reflectance measurement of  $\alpha$ -MnSe powder



*Figure 31. Absorption coefficient of a 162 nm  $\alpha$ -MnSe thin film on a fused silica substrate*

As shown in Figure 32, the MnSe<sub>2</sub> film achieves a  $10^5$  cm<sup>-1</sup> absorption coefficient within 1 eV of the 1.1 eV band gap. This film was approximately 100 nm thick, causing the sub-gap features to be washed out by the lack of signal difference between the reference and the film. A 350 nm film was used to confirm the band gap and rapid turn on of absorption.

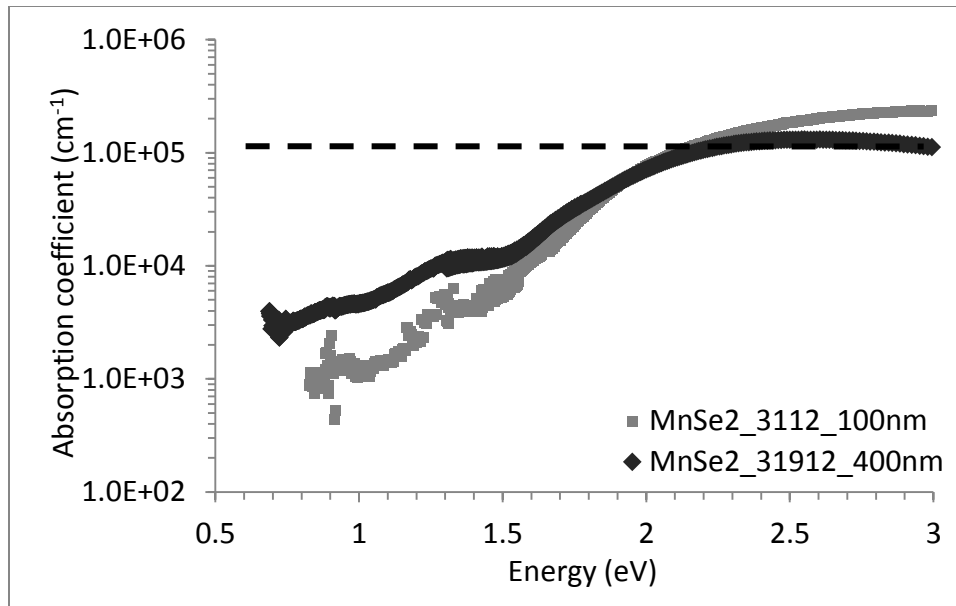


Figure 32. Absorption coefficient measurement of a 100 nm thick MnSe<sub>2</sub> thin film on a fused silica substrate

Seebeck measurements of both a 150 nm  $\alpha$ -MnSe film and 100 nm MnSe<sub>2</sub> film were taken. Both films exhibited p-type conduction. The carrier concentrations within the films were  $>10^{19} \text{ cm}^{-3}$ . Hall measurements of these same films failed to measure a consistent mobility, suggesting low mobility films. Finally, conductivity of both films was found to be 6 ohm·cm.

Table 1 is a summary of the properties characterized in this section.

Table 1. Measured properties of MnSe and MnSe<sub>2</sub> films

Film	Band gap (eV)	$>10^5 \text{ cm}^{-1}$ Absorption	Seebeck coefficient ( $\mu\text{V/K}$ )	Resistivity (ohm·cm)
$\alpha$ -MnSe	1.77	$E_g + 1.23 \text{ eV}$	307	6
MnSe <sub>2</sub>	1.1	$E_g + 1 \text{ eV}$	354	1.7

### 3.4 Discussion

$\text{MnSe}_2$  demonstrates excellent absorption because it follows many of the design principles outlined in the introduction. Looking at the pDOS in Figure 33, the manganese d orbitals are the dominant character in both the valence and the conduction bands. While d-d transitions are not Laporte allowed, they still contain a number of states, narrow energy range, and steep turn on that help electron promotion and the turn on of absorption. Moreover, the selenium p orbitals in the conduction band suggest that d-p allowed transitions contribute to the high absorption.

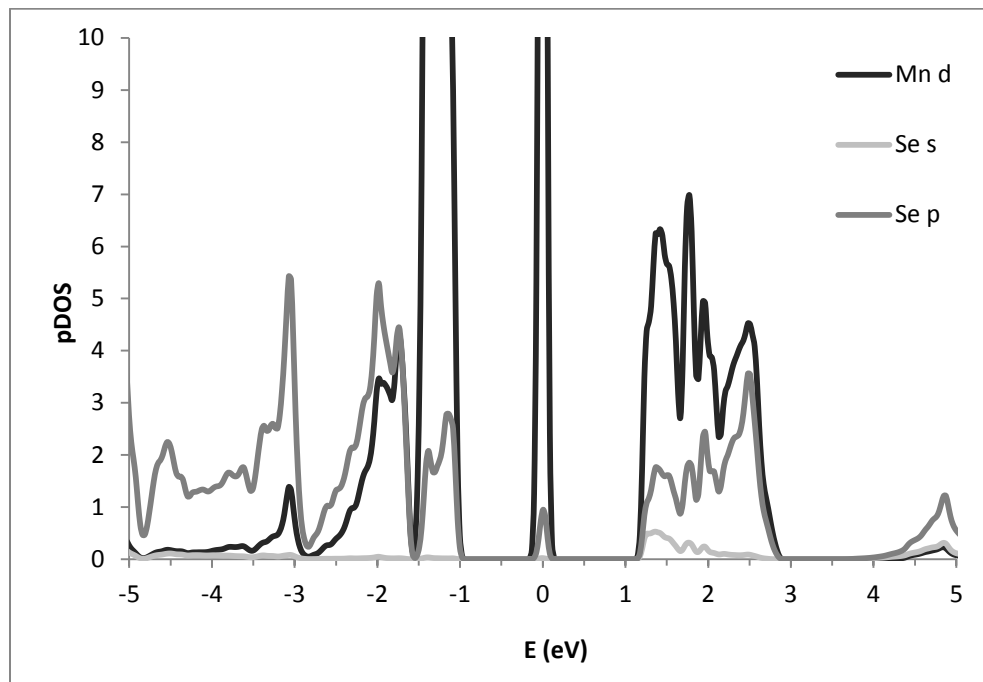
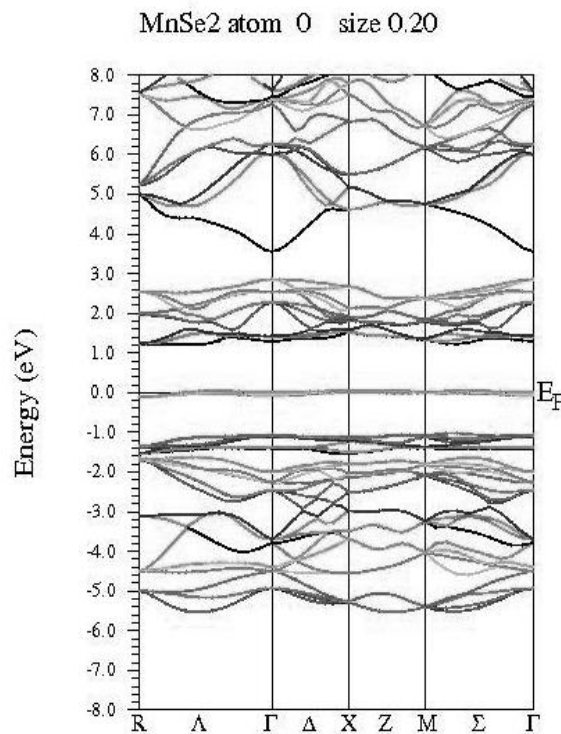


Figure 33.  $\text{MnSe}_2$  DOS diagram

The DFT calculated band gap of 1.1 eV using the GGA+U approximation for MnSe<sub>2</sub> closely matches experimentally measured value. The band diagram of MnSe<sub>2</sub> is presented in Figure 34. Flat bands in both the valence and conduction band make this a direct gap material with a large number of available states.



*Figure 34. Estimated band structure diagram of MnSe<sub>2</sub>. The unusually flat bands at the Fermi level suggest that more correction factors are needed in the calculation. Additional calculations are underway.*

$\alpha$ -MnSe, the proposed potential impurity state of MnSe<sub>2</sub>, shows poor absorption properties, but the low conductivity and high band gap assures that it would be a semiconducting impurity. Figure 35, the predicted  $\alpha$ -MnSe DOS diagram, helps explain the poor absorption and slow turn on. While the valence

band contains significant d character from the manganese, the conduction band is also primarily d-orbital derived and corresponding transitions are Laporte forbidden, hence the low absorption near the band gap in the thin film.

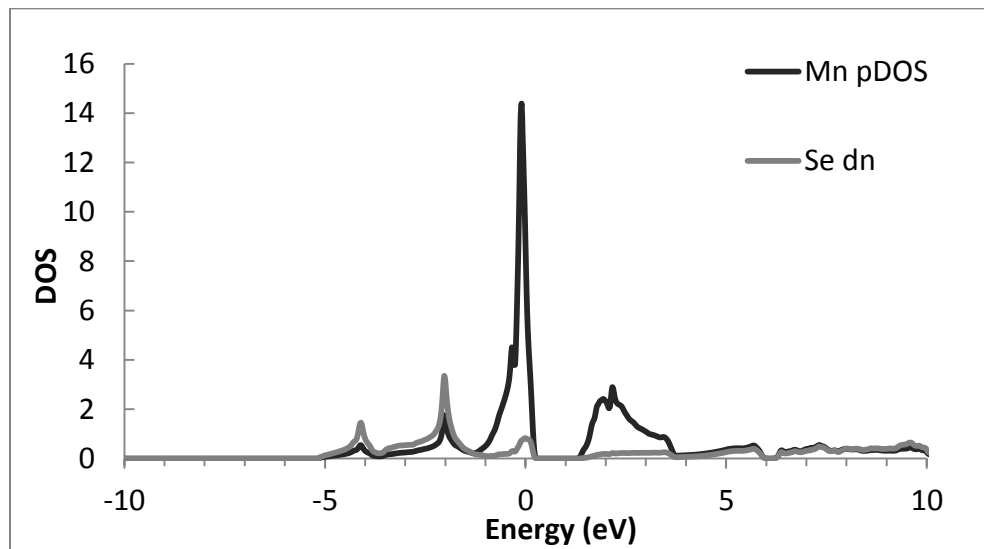


Figure 35.  $\alpha$ -MnSe DOS diagram

The predicted band structure of  $\alpha$ -MnSe, shown in Figure 36, contains an indirect gap with a large energy difference between the first level of the conduction band and the second. The predicted band gap of 1.1 eV is much smaller than the experimentally found gap of 1.77 eV. Band gap is one of the less accurately predicted values in DFT calculations. However, the shape and position of the bands are independent of the accuracy of the band gap, so these are assumed to be correctly predicted. In fact, the band structure shape fits the experimental data well, as a second take off of absorption occurs at 2.3 eV. This jump matches the large energy difference between the first and third conduction bands in the band structure diagram.

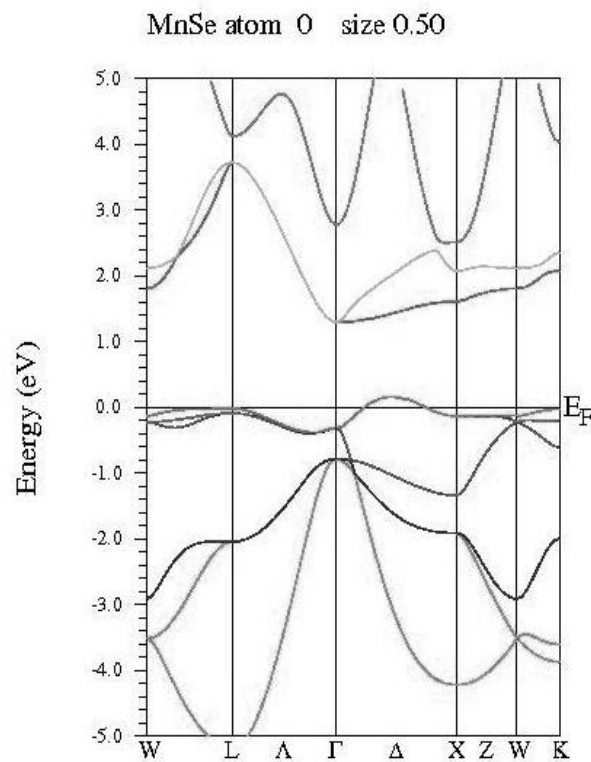


Figure 36. Band diagram of  $\alpha$ -MnSe

### 3.5 MnSe<sub>2</sub> as a solar absorber and future work

MnSe<sub>2</sub> has demonstrated excellent potential for use as a solar absorber. The 1.1 eV band gap and  $>10^5 \text{ cm}^{-1}$  absorption coefficient within 1 eV of the band gap are all suggestive that this material should be further developed.

The low measured mobility and high carrier concentrations in the MnSe<sub>2</sub> film are the only troublesome results in this otherwise excellent solar absorber candidate. Given the roughness of the film, this could be a result of grain boundaries and charge traps. Therefore, to understand the real potential of this system, single crystals of MnSe<sub>2</sub> must be grown and characterized electrically.

During the course of this research, several attempts at synthesizing phase pure  $\text{MnSe}_2$  powder and single crystals were made. Initially, synthesis of  $\text{MnSe}_2$  powder was attempted by combining elemental manganese and selenium in an air evacuated ( $10^{-3}$  torr) sealed fused silica tube. Variations in heating/cooling rate, reaction temperature and stoichiometry were attempted, but the resulting powder always contained at least some  $\text{MnSe}$  impurity that was measurable by XRD analysis. Chemical vapor transport with an iodine transport agent was equally unsuccessful in producing either single phase powder or single crystals.

Hydrothermal synthesis is the most promising routes to achieving  $\text{MnSe}_2$  single crystals with successful growth previously reported [38]. Hydrothermal synthesis, however, generally produces small crystals that would be difficult to measure with traditional contacts, making this method non-trivial.

$\text{MnSe}_2$  single crystals and films could be evaluated by photoelectrochemical (PEC) measurements. This experiment would provide a real measurement of the photoconductivity within the cell. In fact, these measurements were done on a similar structure,  $\text{Mn}_2\text{GeSe}_4$ . Both  $\text{MnSe}_2$  and  $\text{Mn}_2\text{GeSe}_4$  contain edge sharing Mn-Se octahedra. The relationship between these materials is similar to that of the proposed alternative to  $\text{FeS}_2$  by using the material  $\text{Fe}_2\text{GeS}_4$ . The measurement of  $\text{Mn}_2\text{GeSe}_4$  resulted in a clear photoresponse, but a high resistivity in the crystal disrupted the measurement of the photocurrent. Appendix B elaborates more on this experiment.

Overall, low mobility appears to be a threat to the  $\text{MnSe}_2$  system. However, a high absorbing material has a reduced dependency on mobility by allowing for very thin films in the solar cell. Instead, the difficulty in making high quality thin films is the biggest threat to any absorbing material.  $\text{MnSe}_2$  is set

apart not only by the readily achievable phase purity of the thin film, but also by lacking destructive impurity phases.

Thus,  $\text{MnSe}_2$  has been shown to be a promising material for use as a solar absorber and continued study of this material is recommended.

## Chapter 4 CuTaS<sub>3</sub> Characterization and Solar Absorption Properties

### 4.1 Introduction

In a continued effort to use design principles to guide experiments that will ultimately be used to develop novel thin film inorganic solar absorbers, CuTaS<sub>3</sub> was proposed as a viable material for experimental study. This material was first synthesized by Crevecoeur et al. in 1964 [39]. Sunshine and Ibers redetermined the structure in 1987 [40], but the properties remained uninvestigated until SLME calculations at NREL suggested this material would have excellent absorbing properties and an optical band gap of 1.4 eV that is ideal for solar absorption.

In this section, the calculated electronic structure of CuTaS<sub>3</sub> will be presented and related to the previously discussed solar absorption design principles. Synthesis, structural, electrical, magnetic and thin film absorption characterization will be presented to corroborate theory, expand understanding of this relatively obscure material, and even correct errors in the literature about it. Finally, a future direction for CuTaS<sub>3</sub> research will be proposed.

### 4.2 Calculations

Before laboratory experimentation began, CuTaS<sub>3</sub> was evaluated according to the design principles outlined in the introduction.

Using DFT, the density of states around the band gap was calculated (Figure 37). The Cu d and S p are shown to make up the valence band, while the Ta d makes up the conduction band. The steep slope of particularly the S 3p states translates to flat bands that create a larger channel for electron

promotion. This translates to a sharper turn on of absorption. The band gap incorporates spin and Laporte allowed p-d transitions as well as spin allowed, but Laporte forbidden d-d transitions.

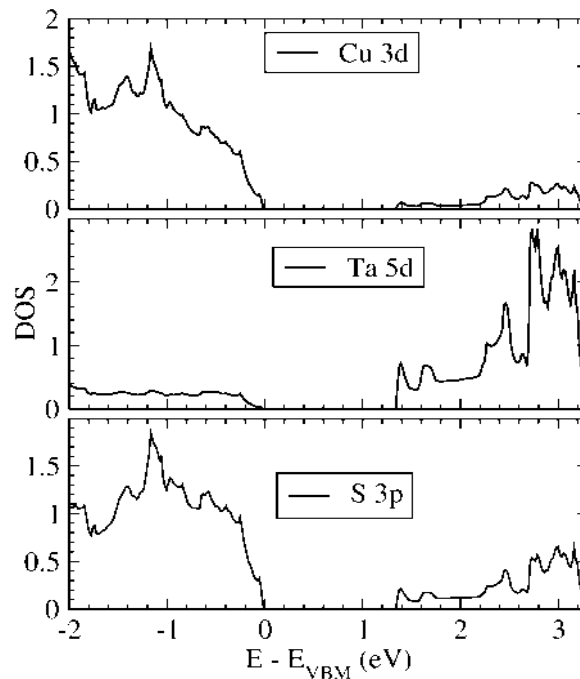


*Figure 37. Density of states of CuTaS<sub>3</sub> as calculated using DFT theory.*

Using the DOS, the absorption coefficient,  $\alpha$ , was predicted to be  $>10^5$   $\text{cm}^{-1}$  within 0.5 eV of the band gap for CuTaS<sub>3</sub> as shown in Figure 38. The rapid turn on and high overall absorption coefficient result in 29% predicted efficiency in a 400 nm film (Figure 39)! This is only 4% below the theoretical maximum efficiency of 33% predicted by Shockley-Queisser [6]. In fact, since this calculation uses an SLME model, which incorporate the real turn on of absorption rather than assuming ideal turn on, this prediction is all the more powerful because it is more accurate to the material.

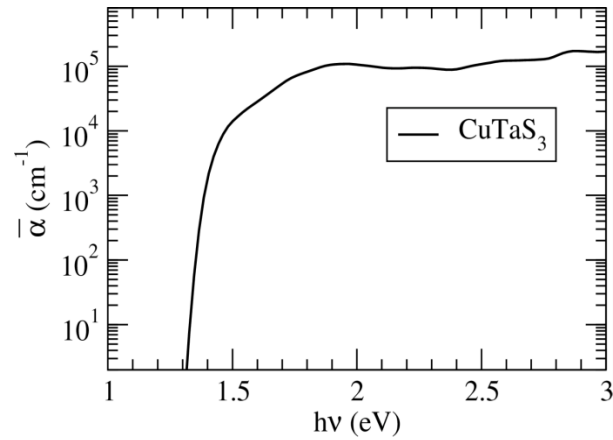


Figure 38. The calculated absorption coefficient of  $\text{CuTaS}_3$  shows that within 0.5 eV of the band gap, greater than  $10^5 \text{ cm}^{-1}$  absorption is possible.

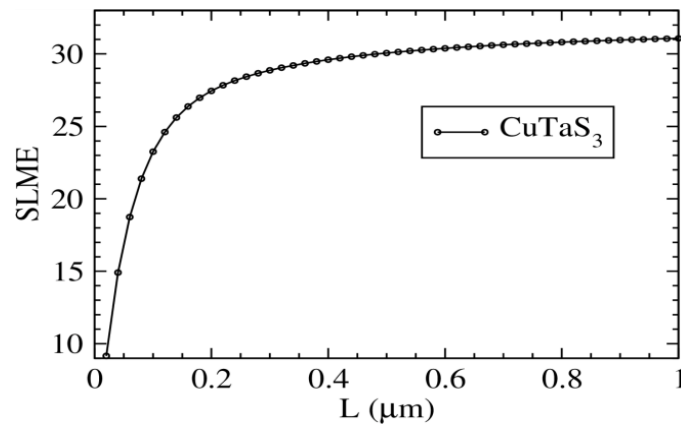


Figure 39. SLME calculations suggest that because of the rapid absorption turn on and  $>10^5 \text{ cm}^{-1}$  absorptivity,  $\text{CuTaS}_3$  has a maximum efficiency of 31%. This is close to the Shockley-Queisser[6] theoretical limit of 33% efficiency.

An examination of the structure and prediction of the electrical properties yields equally promising results. Copper sulfides are actually well known solar absorbers [41] [42], while tantalum sulfides are conductors (even

superconductors at low temperatures [43]). In fact,  $\text{Cu}_x\text{S}$  structures have been predicted to have band gaps between 1.2 and 2.0 eV [41] and demonstrated gaps of 1.2 and 1.8 eV [42]. Copper sulfide based solar cells are not commercially available because copper diffuses into the surrounding layers thus destroying the cell [44]. In this system, tantalum octahedra could stabilize the structure. In fact,  $\text{CuTaS}_3$  can be considered a marriage of two materials as it intertwines copper sulfide tetrahedra with tantalum sulfide octahedra. Therefore, a route to not only excellent absorption, but also promising electrical properties is predicted.

Overall, close examination of the electronic and chemical structures within  $\text{CuTaS}_3$  as they relate to the design principles outlined in the introduction suggest that this material is an excellent candidate for use as a solar absorber.

### **4.3 Synthesis**

$\text{CuTaS}_3$  powder was synthesized by combining stoichiometric amounts of Cu, Ta and S in an air evacuated ( $10^{-3}$  torr) sealed fused silica tube and heating the tube at  $0.5^\circ\text{C}/\text{min}$  to  $650^\circ\text{C}$ . The reaction was allowed to proceed for 7-8 days and cooled at  $1^\circ\text{C}/\text{min}$  to room temperature. The resulting black powder was found to be phase pure by XRD analysis. Shorter reaction times and lower reaction temperatures yielded  $\text{Cu}_3\text{TaS}_4$  impurities.

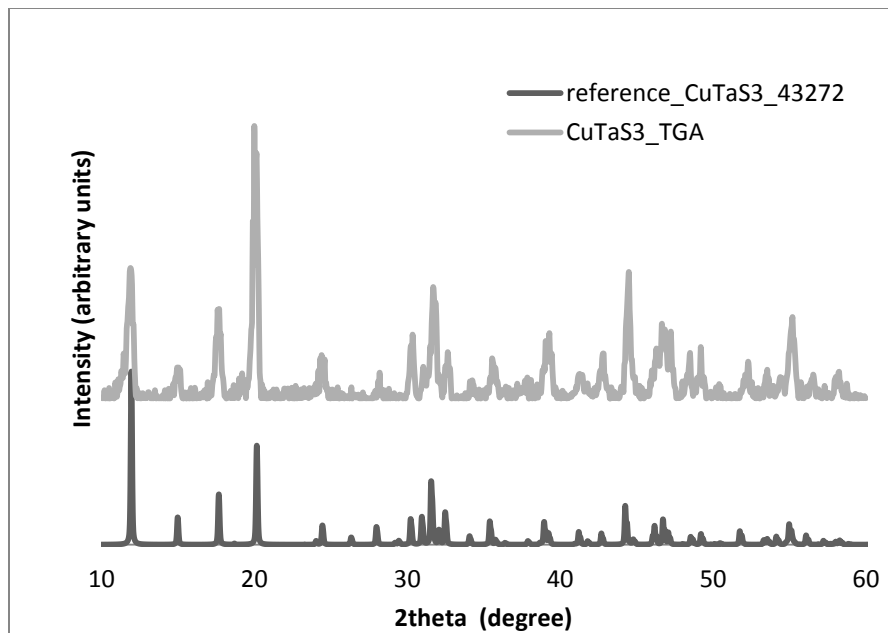


Figure 40. X-ray diffraction pattern of  $\text{CuTaS}_3$  powder synthesized at  $650^\circ\text{C}$ .

Single crystals of  $\text{CuTaS}_3$  were synthesized in two similar manners. A mat of single crystals can be grown by repeating the powder synthesis with the addition of trace amounts of iodine in the tube. Alternatively, long, isolated single crystals can be grown by chemical vapor transport in a three zone furnace. In this method, stoichiometric amounts of Cu, Ta and S are combined in an air evacuated ( $10^{-3}$  torr) sealed fused silica tube with trace amounts of iodine. The powder end of the tube is placed in zone 1, which was heated to  $750^\circ\text{C}$  over the course of 12 hours. After 72 hours, zone 1 was cooled to  $650^\circ\text{C}$  over the course of 3 hours and maintained at this temperature for 99 hours. A 48 hour cool to room temperature then completed the reaction conditions. Concurrently, zone 2 was heated at  $0.81^\circ\text{C}$  to  $750^\circ\text{C}$  and maintained at this temperature for 72 hours. Zone 2 was subsequently cooled to  $700^\circ\text{C}$  over the course of 3 hours, where it

remained for 99 hours. A 48 hour cool to room temperature then completed the reaction conditions. Finally, zone 3 was heated concurrently at 0.6°C/min to 750°C, where it remained for 171 hours, before cooling over the course of 48 hours to room temperature. In this three zone synthesis, a mat of CuTaS<sub>3</sub> single crystals and powder form in zone 3 while longer, isolated crystals grow in zone 1. Single crystal XRD was used to confirm the structure of the single crystals, which match the pattern obtained by Sunshine and Ibers [40].

Thin films were synthesized by electron beam physical vapor deposition of copper and tantalum targets. Depositions were calibrated using in situ thickness measurements to deposit a film of copper on tantalum at a 1:1 atomic ratio resulting in films that are 24 nm copper on 40 nm tantalum. The resulting films were immediately sealed in an air evacuated ( $10^{-3}$  torr) tube with 122±3 mg of sulfur powder and heated at 2°C/min to 650°C. After 1 hour, the films were cooled at a rate of 3°C/min with a slight temperature gradient over the length of the tube.

The final film was confirmed to be CuTaS<sub>3</sub> by XRD analysis using a 150A, 50 kW Cu  $\alpha$  source and 2D detector that allow for excellent pattern strength on even sub-100 nm films. The pattern is shown in Figure 41.

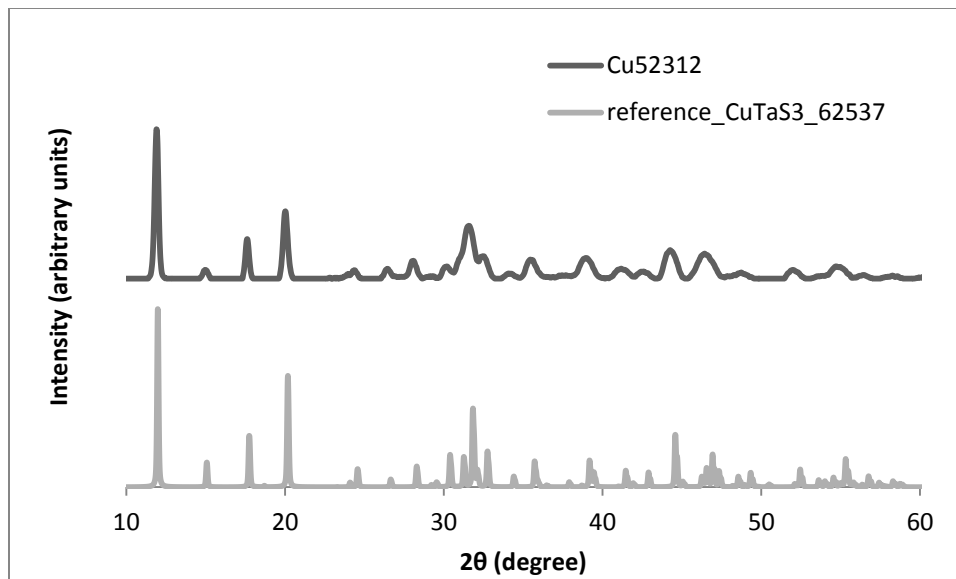
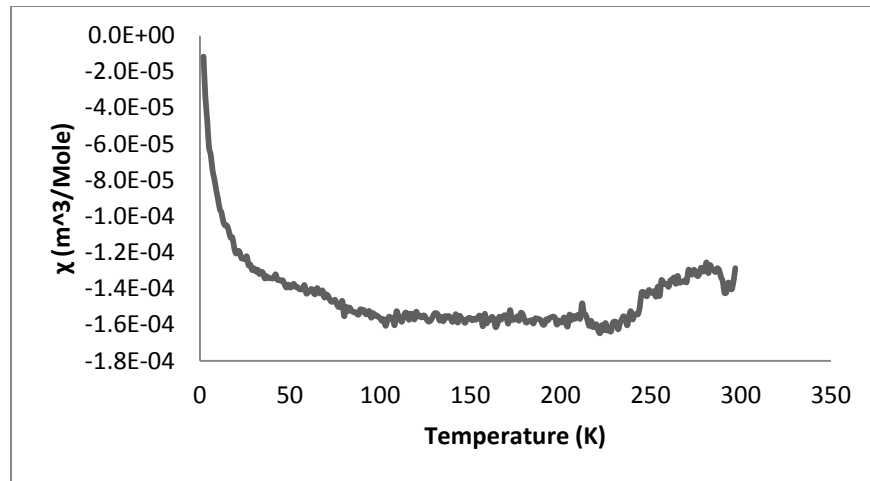


Figure 41. XRD pattern of a  $\text{CuTaS}_3$  thin film.

#### 4.4 Characterization

Magnetic measurements were made by grinding up single crystals of  $\text{CuTaS}_3$  and pressing them into a pellet. A 5000 Oe field was applied over a temperature range of 5K – 300 K. As shown in Figure 42, the resulting magnetic susceptibility remained repulsive for the duration of the experiment indicating that  $\text{CuTaS}_3$  is diamagnetic.



*Figure 42. Magnetic susceptibility plot of CuTaS<sub>3</sub>. The negative susceptibility corresponds to diamagnetic behavior.*

The Seebeck coefficient was measured on several CuTaS<sub>3</sub> single crystals. The measured Seebeck coefficient range of -860 – -1400 indicates that CuTaS<sub>3</sub> is an n-type semiconductor with a carrier concentration between  $10^{16}/\text{cm}^3$  and  $10^{18}/\text{cm}^3$  [45]. A sulfur deficiency is the likely cause of the n-type conductivity. Four-probe conductivity measurements using indium contacts resulted in an average conductivity of 0.02/ohm·cm, with good agreement between samples. The electron mobility was then calculated from these two measurements to be between 0.15 and 15  $\text{cm}^2/\text{V}\cdot\text{s}$ .

Diffuse reflectance measurements of a cluster of CuTaS<sub>3</sub> single crystals are shown in Figure 43. Over the range of 0.5 – 5 eV, a sharp increase in  $k/S$  is seen at 0.92 eV.

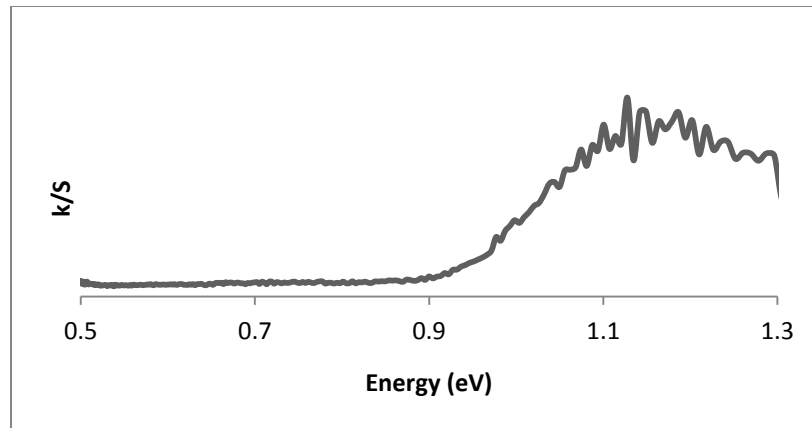


*Figure 43. Diffuse reflectance measurement of CuTaS<sub>3</sub> shows a 0.9 eV band gap. This is significantly lower than the 1.37 eV band gap predicted by density functional calculations.*

By measuring the transmission and reflection of a CuTaS<sub>3</sub> thin film on fused silica and applying Beer's law, the absorption coefficient was calculated with the results shown in Figure 44. A slightly higher band gap of 1 eV is demonstrated as well as a rapid turn on of absorption. In fact, this ~150 nm thick film demonstrated  $>10^5 \text{ cm}^{-1}$  absorption within 0.4 eV of the band gap. The shape and turn of the absorption closely resemble the predicted absorption, shown in Figure 38. Sub-gap absorption, however, is on the order of  $2.6 \times 10^4 \text{ cm}^{-1}$ , suggesting poor film quality.

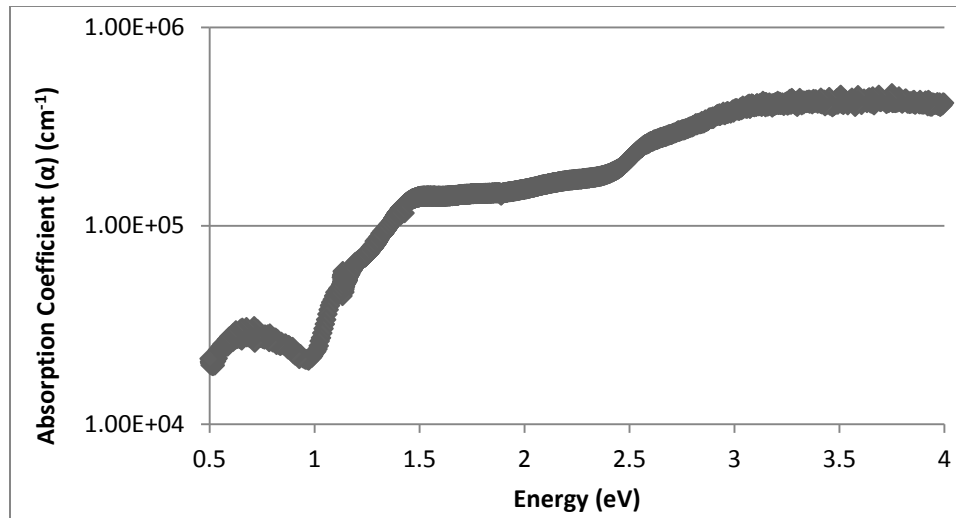
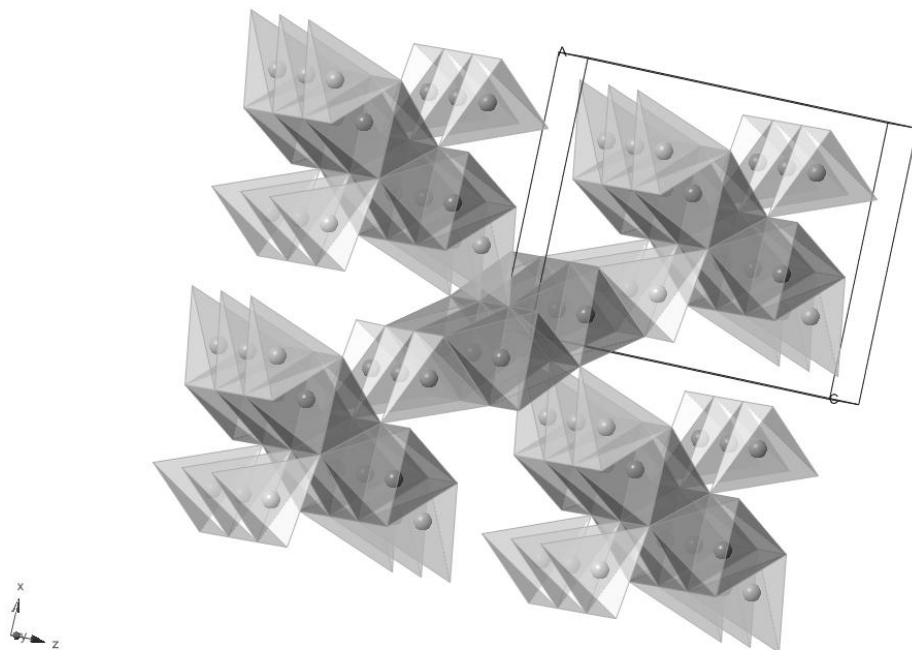


Figure 44. The measured absorption of a  $\text{CuTaS}_3$  thin film

## 4.5 Results and discussion

### 4.5.1 Structure

$\text{CuTaS}_3$  is an orthorhombic structure with tetrahedrally coordinated copper and octahedrally coordinated tantalum in the  $Pnma$  space group. Copper and tantalum are only 2.79 Å apart, suggesting bonding between these elements [39]. The Ta-S octahedra are found in  $y$ -directional double chains, linked by edges. Cu-S tetrahedra link the Ta-S chains together by both edge and corner sharing to create a continuous lattice along the  $x$ - $z$  plane. Based on the chain, a significant increase in conduction is expected along the  $y$ -axis.



*Figure 45.  $\text{CuTaS}_3$  structure is shown with the copper sulfide tetrahedra a lighter shade than the tantalum sulfide octahedra.*

Previous structure reports suggest that  $\text{CuTaS}_3$  consists of Cu(II) and Ta(IV) [39][40]. However, DFT calculations predict that Ta d bands make up the conduction band while the lower energy Cu d bands make up the valence band shown in Figure 37. Therefore, it is unlikely that electrons would populate the higher energy Ta, while a lower energy Cu d orbital remains unfilled. Magnetic susceptibility measurements show that  $\text{CuTaS}_3$  lacks any unpaired electrons and cannot be composed of Ta 5d<sup>1</sup> and Cu 3d<sup>10</sup>. Lacking any other reasonable oxidation states for Cu and Ta, this compound must be composed of Cu(I) and Ta(V).

#### 4.5.2 Solar absorber candidate

CuTaS<sub>3</sub> incorporates the spin and Laporte allowed transitions of p->d and an excellent band gap for solar absorption, making it an auspicious material for further study. The d10 configuration of copper(I) allows for maximum population of the valence band. Electrical measurements of CuTaS<sub>3</sub> single crystals show descent conductivity and reasonable carrier concentrations.

#### 4.5.3 Conclusions

Theory and experiments indicate that the high absorption coefficient caused by the narrow bands, and a band gap that allows for the absorption of 84% of the energy from the solar spectrum, make CuTaS<sub>3</sub> an excellent candidate for a solar absorber. Phase pure powders and single crystals were grown in evacuated sealed tubes and with a chemical transport agent being employed for crystal growth. Magnetic susceptibility measurements reveal that CuTaS<sub>3</sub> is diamagnetic, thereby demonstrating that CuTaS<sub>3</sub> is composed of Cu(I) and Ta(V), not the previously reported Cu(II) and Ta(IV). Electrically, CuTaS<sub>3</sub> single crystals are n-type semiconductors with a carrier concentration between 10<sup>16</sup>/cm<sup>3</sup> and 10<sup>18</sup>/cm<sup>3</sup>. The conductivity was measured to be 0.02/ohm·cm leading to a calculated mobility between 0.15 and 15 cm<sup>2</sup>/V·s. The most intriguing unknown, the absorption coefficient of CuTaS<sub>3</sub>, is demonstrated to have a rapid that leads to >10<sup>5</sup> cm<sup>-1</sup> absorption within 0.4 eV of the 1.1 eV band gap.

#### 4.6 Future Work

Future work should focus on creating high quality thin films of CuTaS<sub>3</sub>. The films used to measure the absorption coefficient were not electrically conductive, suggesting a non-uniform film. Like other copper based solar

absorbers, the challenge to this material is maintaining film stoichiometry [46]. In developing a synthetic method to a phase pure  $\text{CuTaS}_3$  film, the high melting point of tantalum and need to carefully control the stoichiometry in order to avoid the impurity phase  $\text{Cu}_3\text{TaS}_4$  were a constant challenge. Moreover, the ready oxidation of both copper and tantalum meant that minimizing exposure of unsulfurized films was necessary. While some success was achieved in all of these areas, much more is both possible and necessary. Finally, film adhesion should be improved in order to create a more electrically active film.

All of the proposed future work is thought to be readily attainable with skillful lab technique. As this material has presented excellent absorbing properties, it is strongly recommended that  $\text{CuTaS}_3$  be further investigated for use as a solar absorber.

## Chapter 5 Conclusions

Three transition metal chalcogenides were investigated for their potential as solar absorbers. Through the investigation, a set of design principles was constructed and each material was investigated in the context of these design principles as well as in an overall systemic approach in which impurities and potential problems were considered. The design principles state that low oxidation state transition metal can better populate the valence band leading to higher absorption (ex. Cu(I) has the d10 configuration). Second, that spin and Laporte allowed d → p transitions take advantage of the large number of available states offered by d and p orbitals and high probability of excitation. Spin allowed transitions that do not change in multiplicity, such as if all of the  $t_2$  electrons transition to three empty states in the  $E_{\text{cond}}$ , increase the chances of absorption. However, even d-d transitions are capable of producing high absorption because of the large number of states in high quantum number orbitals. Third, the smaller the  $\Delta E$  between the vacuum and valence electrons, the more easily an electron can escape the attraction of the nucleus. Fourth, the  $E_g = E_{\text{con}} - E_{\text{val}} \propto J_{\text{oc}}$  of the solar cell, should be in range to absorb the maximum solar radiation. Fifth, more orbitals in a narrower energy range encourage a more rapid turn on of absorption. Finally, a systematic approach is needed to best understand the real potential of a semiconductor to be used as a solar absorber. The ultimate irony would be to have a solar absorber that breaks down when exposed to radiation.

The 1 eV band gap of iron pyrite and  $>10^5 \text{ cm}^{-1}$  absorption coefficient within 0.5 eV of the band gap suggest that this material would be a good solar

absorber. It combines a low oxidation state transition metal with the large number of states in d-d transitions. However, pyrite demonstrates poor electrical properties due to energetically favorable metallic impurities. Manganese diselenide was found to be a suitable alternative to iron pyrite, as any loss of the chalcogenide would maintain the semiconductivity of the material. A better understanding of the mobility of manganese diselenide is needed. Finally,  $\text{CuTaS}_3$ , follows all of the design principles and demonstrates correspondingly excellent absorption. The synthesis of high quality thin films is the next step to exploring this promising material.

## BIBLIOGRAPHY

- [1] P. A. Tipler and G. Mosca, *Physics For Scientists and Engineers*, 6th ed. W. H. Freeman and Company, 2008.
- [2] M. Fogiel, "Reflectance," in *The Optics Problem Solver*, New York, NY: Research and Education Association, 1987.
- [3] NREL, "Solar Spectra: Air Mass Zero," *Renewable Resource Data Center*. [Online]. Available: <http://rredc.nrel.gov/solar/spectra/am0/>. [Accessed: 23-Jan-2012].
- [4] R. Xu, W. Pang, and Q. Huo, *Modern Inorganic Synthetic Chemistry*. Elsevier, 2011.
- [5] T. Trupke, M. A. Green, and P. Würfel, "Improving solar cell efficiencies by down-conversion of high-energy photons," *Journal of Applied Physics*, vol. 92, no. 3, p. 1668, 2002.
- [6] W. Shockley and H. J. Queisser, "Detailed Balance Limit of Efficiency of p-n Junction Solar Cells," *Journal of Applied Physics*, vol. 32, no. 3, p. 510, 1961.
- [7] A. D. Vos, "Detailed balance limit of the efficiency of tandem solar cells," *Journal of Physics D: Applied Physics*, vol. 13, p. 839, 1980.
- [8] D. F. Shriver, P. W. Atkins, T. L. Overton, J. P. Rourke, M. T. Weller, and F. A. Armstrong, *Inorganic Chemistry*, Fourth. New York, NY: W. H. Freeman and Company, 2006.
- [9] R. Sun, M. Chan, and G. Ceder, "First-principles electronic structure and relative stability of pyrite and marcasite: Implications for photovoltaic performance," *Physical Review B*, vol. 83, no. 23, Jun. 2011.
- [10] L. Yu and A. Zunger, "Identification of Potential Photovoltaic Absorbers Based on First-Principles Spectroscopic Screening of Materials," *Physical Review Letters*, vol. 108, Feb. 2012.
- [11] B. D. Pelatt, R. Ravichandran, J. F. Wager, and D. A. Keszler, "Atomic Solid State Energy Scale," *Journal of the American Chemical Society*, 2011.
- [12] J. A. Spies, R. Schafer, J. F. Wager, P. A. Hersh, H. A. S. Platt, D. A. Keszler, G. Schneider, R. Kykyneshi, J. Tate, X. Liu, and W. N. Shafarman, "pin double-heterojunction thin-film solar cell p-layer assessment," *Solar Energy Materials and Solar Cells*, vol. 93, pp. 1296–1308, 2009.
- [13] F. Hulliger and E. Mooser, "Semiconductivity in pyrite, marcasite and arsenopyrite phases," *Journal of Physics and Chemistry of Solids*, vol. 26, no. 2, pp. 429–433, Feb. 1965.
- [14] A. Ennaoui, S. Fiechter, C. Pettenkofer, N. Alonso-Vante, K. Buker, M. Bronold, C. Hopfner, and H. Tributsch, "Solar energy materials and solar cells," *Solar Energy Materials and Solar Cells*, vol. 29, no. 4, pp. 289–370, 1993.

- [15] R. Sun, M. K. Y. Chan, S. Kang, and G. Ceder, "Intrinsic stoichiometry and oxygen-induced p-type conductivity of pyrite  $\text{FeS}_2$ ," *Physical Review B*, vol. 84, no. 3, Jul. 2011.
- [16] Y. Li, R. A. Van Santen, and T. Weber, "High-temperature  $\text{FeS}$ - $\text{FeS}_2$  solid-state transitions: Reactions of solid mackinawite with gaseous  $\text{H}_2\text{S}$ ," *Journal of Solid State Chemistry*, vol. 181, no. 11, pp. 3151–3162, 2008.
- [17] H. A. S. Platt, "Copper and Iron Chalcogenides for Efficient Solar Absorption," Doctor of Philosophy, Oregon State University, Corvallis, Oregon, 2010.
- [18] L. Yu, S. Lany, R. Kykyneshi, V. Jieratum, R. Ravichandran, B. Pelatt, E. Altschul, H. A. S. Platt, J. F. Wager, A. Zunger, and D. A. Keszler, "Iron Chalcogenide Photovoltaic Absorbers," *Advanced Materials*.
- [19] K. B ker, N. Alonso-Vante, and H. Tributsch, "Photovoltaic output limitation of n- $\text{FeS}_2$  (pyrite) Schottky barriers: A temperature-dependent characterization," *Journal of Applied Physics*, vol. 72, no. 12, p. 5721, 1992.
- [20] C. C. Ahn and O. L. Krivanek, *EELS Atlas*. ASU HREM facility and GATAN.
- [21] M. F. Toney and S. Brennan, "Structural depth profiling of iron oxide thin films using grazing incidence asymmetric Bragg x-ray diffraction," *Journal of Applied Physics*, vol. 65, no. 12, pp. 4763 – 4768, Jun. 1989.
- [22] M. R. Stanton and M. B. Goldhaber, "Experimental Studies of the Synthesis of Pyrite and Marcasite ( $\text{FeS}_2$ ) from 0 to 200 C and Summary of Results," United States Geological Survey, Denver, CO, 91-310, 1991.
- [23] FIZ Karlsruhe, "International Crystal Structure Database." .
- [24] S. Raab, P. Hoth, E. Huenges, and H. J. Muller, "Role of sulfur and carbon in the electrical conductivity of the middle crust," *Journal of Geophysical Research*, vol. 103, no. B5, pp. 9681–9689, May 1998.
- [25] B. Hyde and M. O'Keeffe, "Marcasite and Pyrite ( $\text{FeS}_2$ )," *Australian Journal of Chemistry*, vol. 49, pp. 867–872, 1996.
- [26] M. J. Buerger, "Interatomic distances in marcasite and notes on the bonding in crystals of loellingite, arsenopyrite, and marcasite types," *Zeitschrift fuer Kristallographie*, vol. 97, pp. 504–513, 1937.
- [27] S. Finklea, L. Cathey, and E. L. Amma, "Investigation of the bonding mechanism in pyrite using the moessbauer effect and X-ray crystallography," *Acta Crystallographica A*, vol. 32, pp. 529–537, 1976.
- [28] M. S. Jagadeesh and M. S. Seehra, "Electrical resistivity and band gap of marcasite ( $\text{FeS}_2$ )," *Physics Letters A*, vol. 80, no. 1, pp. 59–61, Nov. 1980.
- [29] A. G. Schaufu , H. W. Nesbitt, I. Kartio, K. Laajalehto, G. M. Bancroft, and R. Szargan, "Incipient oxidation of fractured pyrite surfaces in air," *Journal of Electron Spectroscopy and Related Phenomena*, vol. 96, pp. 69–82, 1998.

- [30] H. W. Nesbitt, M. Scaini, H. Hochst, G. M. Bancroft, A. G. Schaufuss, and R. Szargan, "Synchrotron XPS evidence for Fe<sup>2+</sup>-S and Fe<sup>3+</sup>-S surface species on pyrite fracture-surfaces, and their 3D electronic states," *American Mineralogist*, vol. 85, pp. 850–857, 2000.
- [31] A. N. Buckley, "The surface oxidation of pyrite," *Applied Surface Science*, vol. 27, pp. 437–452, 1987.
- [32] Q. Peng, Y. Dong, Z. Deng, H. Kou, S. Gao, and Y. Li, "Selective Synthesis and Magnetic Properties of  $\alpha$ -MnSe and MnSe<sub>2</sub> Uniform Microcrystals," *The Journal of Physical Chemistry B*, vol. 106, no. 36, pp. 9261–9265, Sep. 2002.
- [33] A. Baroni, "Sul polimorfismo di Mn Se," *Zeitschrift fuer Kristallographie*, vol. 99, pp. 336–339, 1938.
- [34] W. Heimbrodt, O. Goede, I. Tschentscher, V. Weinhold, A. Klimakow, U. Pohl, K. Jacobs, and N. Hoffmann, "Optical study of octahedrally and tetrahedrally coordinated MnSe," *Physica B*, vol. 185, pp. 357–361, 1993.
- [35] L. Cemic and A. Neuhaus, "Ueber eine neue Hochdruckmodifikation des MnSe vom Ni As -Type und ueber die Mischbarkeit Mn Se - Mn Te," *High Temperatures-High Pressures*, vol. 4, pp. 97–99, 1972.
- [36] D. L. Decker and R. L. Wild, "Optical Properties of alpha-MnSe," *Physical Review B*, vol. 4, no. 10, pp. 3425–3437, Nov. 1971.
- [37] V. Thanigaimani and M. A. Angadi, "Optical properties of MnSe thin films," *Thin Solid Films*, vol. 245, pp. 146–151, 1994.
- [38] L. Wang, L. Chen, T. Luo, K. Bao, and Y. Qian, "A facile method to the cube-like MnSe<sub>2</sub> microcrystallines via a hydrothermal process," *Solid State Communications*, vol. 138, no. 2, pp. 72–75, Apr. 2006.
- [39] C. Crevecoeur and C. Romers, "The Crystal Structure of CuTaS<sub>3</sub>," *Proceedings of the Koninklijke Nederlandse Akademie van Wetenschappen, Series B: Physical Sciences*, vol. 67, no. 3, pp. 289–291, 1964.
- [40] Steven A. Sunshine and J. A. Ibers, "Redetermination of the Structures of CuTaS<sub>3</sub> and Nb<sub>2</sub>Se<sub>9</sub>," *Acta Crystallographica*, vol. C43, pp. 1019–1022, 1987.
- [41] Q. Xu, Y. Zhao, Y. Yan, and R. Noufi, "Crystal and electronic structures of CuxS solar cell absorbers," *Applied Physics Letters*, vol. 100, 2012.
- [42] F. Bryant, A. Hariri, S. Salkalachen, and C. Scott, "The electrical characteristics of thin film CuxS-CdS solar cells and their dependence on the ambient atmosphere during annealing," *Journal of Physics D: Applied Physics*, vol. 16, p. 1755, 1983.
- [43] C. W. Dunnill, I. MacLaren, and D. H. Gregory, "Superconducting tantalum disulfide nanotapes; growth, structure and stoichiometry," *Nanoscale*, vol. 2, no. 1, p. 90, 2010.

- [44] V. Jayaraman, "Fabrication and Characterization of CIS/CdS and Cu<sub>2</sub>S/CdS Devices for Application in Nano Structured Solar Cells," University of Kentucky, 2005.
- [45] H. L. Tuller and A. S. Nowick, "Small Polaron Electron Transport in Reduced CeO<sub>2</sub> Single Crystals," *Journal of Physics and Chemistry Solids*, vol. 38, pp. 859–867, 1977.
- [46] H. S. Ullal, "Polycrystalline Thin-Film Solar Cell Technologies," presented at the 18th International Photovoltaic Science and Engineering Conference and Exhibition, Kolkata, India, 2009.
- [47] H.-K. Cho and J. Ahn, "EUV Mask and Mask Metrology," in *EUV Lithography*, Bellingham, WA: SPIE Press, 2009.
- [48] Joshua A. Russell, "Measurement of Optical Bandgap Energies of Semiconductors," Master of Science, Oregon State University, Corvallis, Oregon, 2011.

## Chapter 6 Appendix

### Appendix A – Calculations

#### A.1 Seebeck Coefficient

The Seebeck coefficient, or thermopower, is directly related to the carrier concentration

$$\text{Seebeck Coefficient} \equiv \alpha = -\frac{V_{hot} - V_{cold}}{T_{hot} - T_{cold}} = -\frac{k}{e} \left\{ \ln \beta \left( \frac{1-c}{c} \right) + \frac{S_T}{k} \right\}$$

where  $S_T$  is the vibrational entropy associated with the surrounding ions,  $\beta$  is a correction factor for the spin and orbital degeneracy of the electron carrier, and  $c$  is the fraction of sites that contain an electron. During the measurement, one side of the film is heated and allowed to cool while recording  $\Delta V$  as related to  $\Delta T$ . Once the volume of the unit cell is calculated, this calculation provides a good estimate of the carrier concentration assuming that one electron is permitted per formula unit and all other interaction effects are negligible [45].  $\beta$  is suggested to be 2 for systems in which the charge carriers [47] (P. M. Chaikin, 1976).  $S_T$  is considered to be negligible [45] (H. L. Tuller, 1977). This approximation does not work if  $c \geq 0.1$  because of the interaction effects that occur at such high carrier concentrations.

## A.2 Optics

Evaluating thin film absorption can readily be done by simply subtracting the light that is transmitted and reflected to learn the absorption Equation 1. However, absorption is a thickness dependent property making,  $A$ , or absorption, difficult to compare with other experiments. The absorption coefficient,  $\alpha$ , is a much more powerful measurement because it allows for systems to be compared and thin film interference to be accounted for [48].

$$A = 1 - T - R \quad \text{Equation 1}$$

Thin films must be at least partially transparent (~70% ideally) over the region being measured and on a substrate that is completely transparent over the region being measured. Fused silica and Corning 1737 glass (now Eagle 5000) substrates were found to have suitable optical transparency for the experiments in this thesis. Film roughness disrupts reflectance, thus artificially increasing the measured absorption coefficient.

Measurement of the absorption coefficient was performed by first measuring the reflection of the sample ( $R_{\text{experimental}}$ ), the background reflection ( $R_{\text{dark}}$ ), and the reflection of a calibrated mirror ( $R_{\text{mirror}}$ ), the transmission through air ( $T_{\text{control}}$ ), the background transmission ( $T_{\text{dark}}$ ) and the transmission through the sample ( $T_{\text{experimental}}$ ) at the wavelengths of most interest. Using Equation 2 and Equation 3, the calibrated values of  $T$  and  $R$  were found for each wavelength. The thickness ( $d$ ) was measured in centimeters by alternate methods. The absorption coefficient was then determined using Equation 4. A more detailed description of this method is outlined by Russell [48].

$$R = R_{mirror, std} \left( \frac{R_{experimental} - R_{dark}}{R_{mirror} - R_{dark}} \right) \quad \text{Equation 2}$$

$$T = \frac{T_{experimental} - T_{dark}}{T_{control} - T_{dark}} \quad \text{Equation 3}$$

$$\alpha = \frac{-\ln\left(\frac{T}{1-R}\right)}{d} \quad \text{Equation 4}$$

## Appendix B – $\text{Mn}_2\text{GeSe}_4$ PEC measurements

$\text{Mn}_2\text{GeSe}_4$  crystallizes in the olivine structure type with the Pnma space group symmetry. Like  $\text{MnSe}_2$ , it contains edge sharing Mn-Se octahedra and manganese is in the +2 oxidation state.

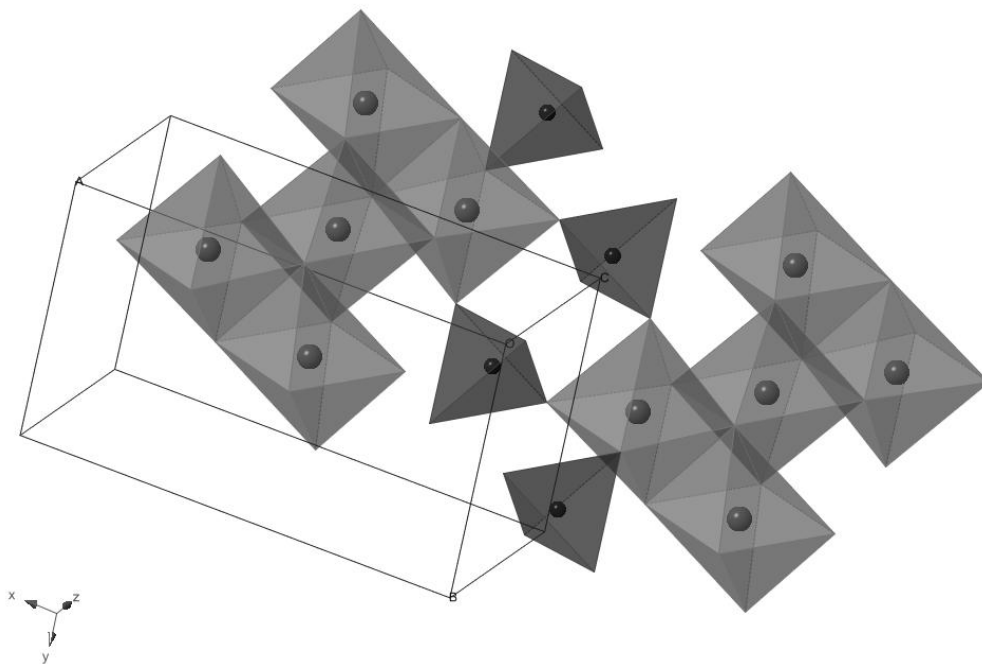


*Figure 46. The crystal structure of  $\text{Mn}_2\text{GeSe}_4$ . The manganese selenide octahedra are lightly shaded, while the germanium selenide tetrahedra are darker.*

### B.1 Synthesis

$\text{Mn}_2\text{GeSe}_4$  powder was synthesized by grinding together manganese, germanium and selenium powders in a ratio of  $\text{Mn}_2\text{GeSe}_5$ . The mixture was sealed in an air evacuated ( $10^{-3}$  torr) sealed fused silica tube. The tube was heated at  $5^\circ\text{C}/\text{min}$  to  $600^\circ\text{C}$ . After 4 days, the tube was allowed to naturally cool

to room temperature. The resulting powder was separated from any excess condensed selenium and found to be phase pure by XRD analysis.

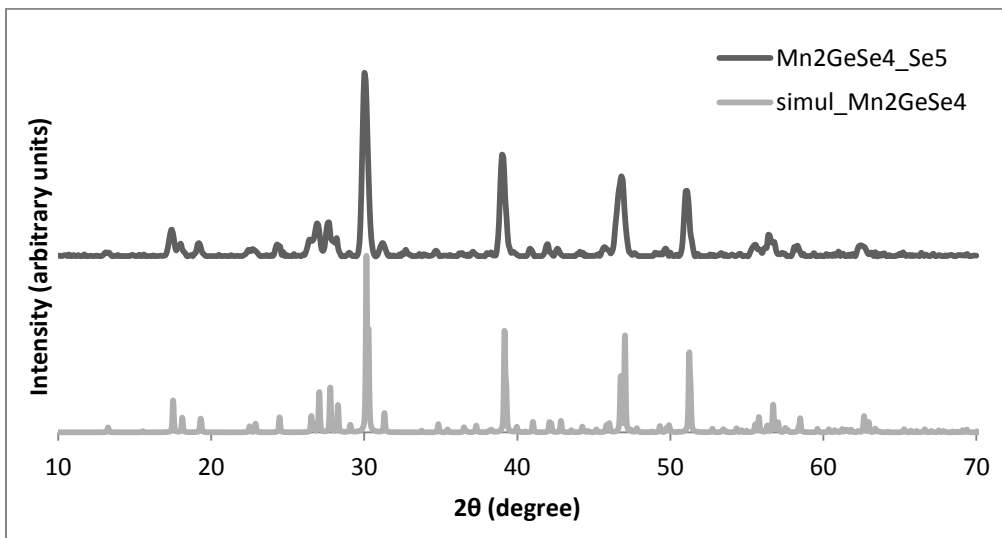


Figure 47. XRD pattern of  $Mn_2GeSe_4$  powder synthesized with an excess of selenium

Single crystals of  $Mn_2GeSe_4$  were synthesized by grinding up  $Mn_2GeSe_4$  powder and sealing it in an air evacuated ( $10^{-3}$  torr) sealed fused silica tube with an iodine transport agent. Two temperature zones were applied across the tube. The powder was placed in the end heated to  $625^\circ C$  and the crystals formed in the  $426^\circ C$  end. The crystals grew in the middle of the tube. Identification of the crystals was confirmed by single crystal XRD.

## B.2 PEC measurements

PEC measurements were performed by evaporating 50 nm gold on the back of a  $Mn_2GeSe_4$  crystal and connecting a wire to this contact point with silver

epoxy (epotek H20E). The crystal and wires were then encased in a glass tube and sealed with a non-conductive epoxy. The only area exposed to the solution in the measurement was a small crystal face. Subsequent measurements were carried out in an inert glovebox using recrystallized/dried reagents. 0.02M cobaltacene (CoCp) and 0.001M  $\text{CoCp}^+$  in 20mL acetonitrile was used as the redox pair. 0.25M tetrabutylammonium hexafluorophosphate (TAHP) was used as the supporting electrolyte to improve ionic conductivity. Light was provided by a 660nm LED ( $100\text{mW cm}^{-2}$ ) that was chopped using a function generator.  $\text{CoCp}^+$  was generated in situ by chemical oxidation using a Pt electrode.

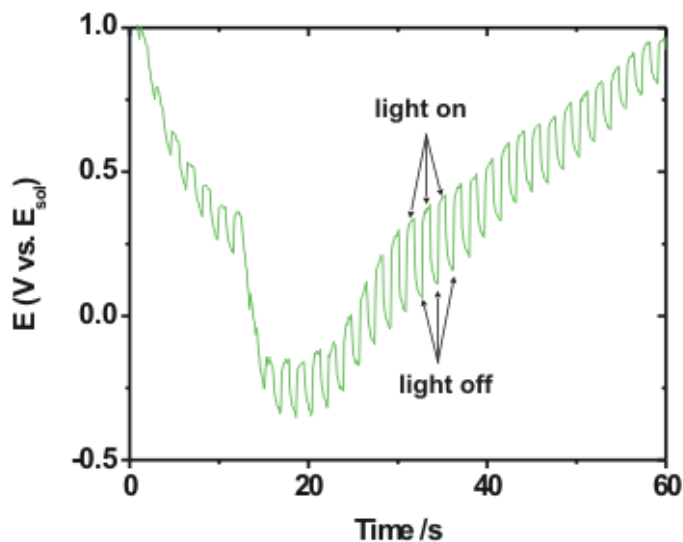


Figure 48. Open circuit voltage PEC measurement of a  $\text{Mn}_2\text{GeSe}_4$  single crystal

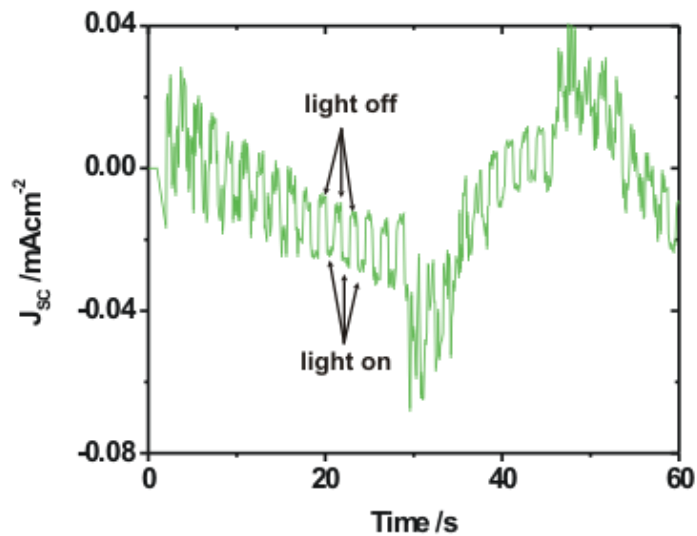


Figure 49. Short circuit current PEC measurement of a  $Mn_2GeSe_4$  single crystal

A clear photoresponse can be seen in Figure 48 and Figure 49 as both the open circuit voltage and short circuit current change when exposed to light. However, high resistance is also demonstrated causing the oscillations in the measurements. A slow build-up of current/voltage is experienced and then slowly dissipated by the  $Mn_2GeSe_4$  crystal. It remains unclear why this capacitor-like behavior is exhibited. Reaction by the crystals with the solution is one possible cause, but the mechanism of such interference is unclear. Low mobility within the crystal is considered the most likely explanation that would cause such a slow dissipation of charge.

## Appendix C – Novel Synthesis of $\text{Bi}_{1.88}\text{Mn}_{0.88}\text{S}_{3.75}$

A novel Mn-Bi-S layered structure was synthesized in single crystal form and characterized using x-ray diffraction. Several misfit layer metal bismuth sulfide defect structures in the space group  $C2/M$  have been reported with a similar  $a$ ,  $b$ ,  $\alpha$ , and  $\beta$  parameters, including a closely related  $\text{Mn}_{0.102(1)}\text{Bi}_{0.320(2)}\text{S}_{0.58(1)}$  single crystal.

### C.1 Synthesis

Manganese, bismuth sulfide and sulfur were combined in an air evacuated ( $10^{-3}$  torr) sealed fused silica tube with an iron bromide transport agent. The ratio of the elements was  $\text{Mn}_2\text{Bi}_2\text{S}_5$ . The tube was placed in a three zone furnace with the powder concentrated in zone 3. Zone 1 was heated to  $700^\circ\text{C}$  over the course of 8 hours. After 62 hours, it was cooled over the course of 8 hours to room temperature. Zone 2 was heated to  $700^\circ\text{C}$  over the course of 8 hours. After 12 hours, this zone was ramped to  $750^\circ\text{C}$  over the course of 3 hours. After 50 hours, a 12 hour cool to room temperature was initiated. Zone 3 was ramped to  $700^\circ\text{C}$  over the course of 12 hours. After a 12 hour soak, a 3 hour ramp to  $800^\circ\text{C}$  was initiated. Zone 3 remained at  $800^\circ\text{C}$  for 50 hours and allowed to cool to room temperature over the course of 12 hours. The  $\text{Bi}_{1.88}\text{Mn}_{0.88}\text{S}_{3.75}$  grew in zone 1.

### C.2 Characterization

Full data collection of a  $\text{Bi}_{1.88}\text{Mn}_{0.88}\text{S}_{3.75}$  single crystal was taken by XRD. EDX was used to estimate elemental composition and the results are shown in Table 2.

Table 2. EDX elemental analysis of a  $\text{Bi}_{1.88}\text{Mn}_{0.88}\text{S}_{3.75}$  single crystal

Element	Weight %	Atomic %
BrL	1.29	1.36
S K	22.22	58.07
MnK	8.81	13.44
BiL	67.67	27.13
Total	100	100

SEM images of a cluster of  $\text{Bi}_{1.88}\text{Mn}_{0.88}\text{S}_{3.75}$  crystals are shown in Figure 50.

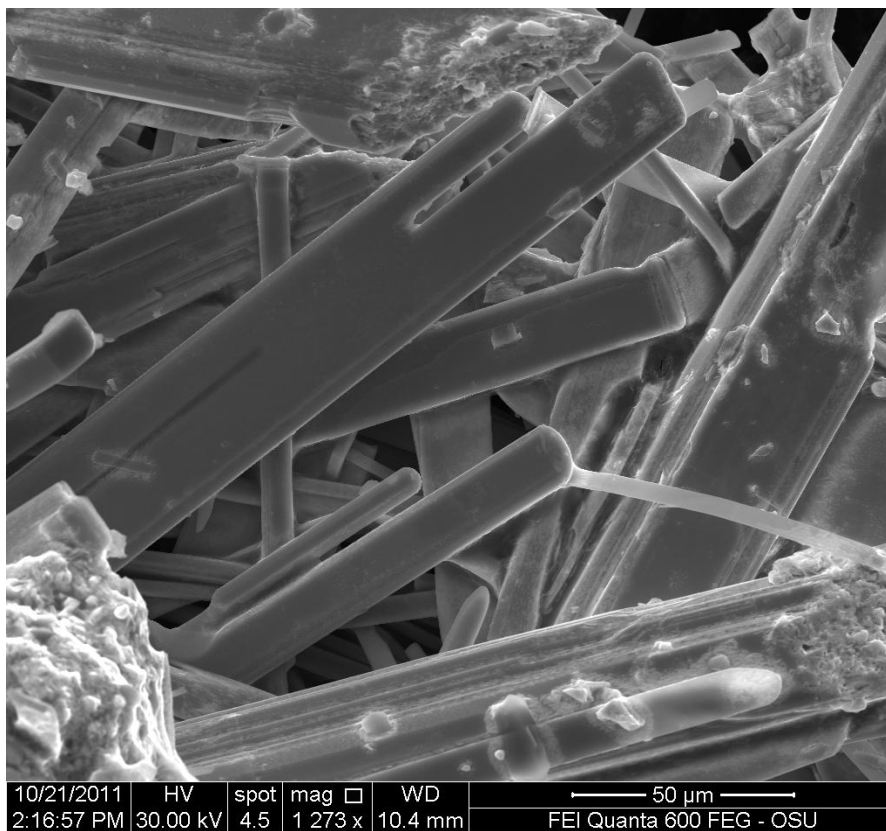


Figure 50. SEM Image of  $\text{Bi}_{1.88}\text{Mn}_{0.88}\text{S}_{3.75}$  crystals

XRD structure determination found that the bromine was not incorporated into the structure. The bromine detected by EDX analysis is therefore assumed to be some of the transport agent that is on the surface of the crystals.

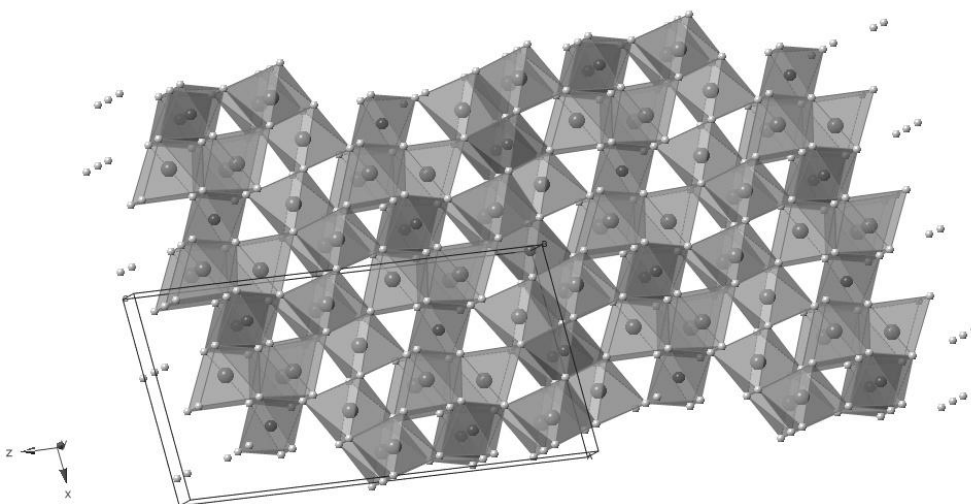


Figure 51. Crystal structure of  $\text{Bi}_{1.88}\text{Mn}_{0.88}\text{S}_{3.75}$ .

A centrosymmetric misfit layered structure based on the NaCl structure type,  $\text{Bi}_{1.88}\text{Mn}_{0.88}\text{S}_{3.75}$  consists of octahedrally coordinated Mn(II) and Bi(III). The reactants contained higher manganese content than the single crystal. This overpressure is suspected to have caused the addition of a defect Bi/Mn layer that consists of regular octahedron to the previously reported  $\text{Mn}_{0.7}\text{Bi}_{2.2}\text{S}_3$  structure.

While Bi(1) retains a slightly distorted octahedral coordination, Bi(2) and Bi(3) are 7-coordinate by bond lengths ranging from 2.4 – 3.6 and monocapped octahedron. This distortion creates a space that only Mn(1) occupies in a square planar configuration. Bi(4) has only one irregular bond length in its 6-coordinate

environment, thereby allowing for Mn to intermix at these sites. Bi(5) is an undistorted octahedrally coordinated site, and continues this trend of allowing Mn(II) to intermix. The soft, electron abundant bismuth can distort to fill the space, while only fairly symmetric sites contain the mixed occupancy Mn(II).